White-Light Imaging Interferometry

by

Sara Vanessa Fernandez

M.MSc., Tsinghua University (2024)
B.S. Massachusetts Institute of Technology (2023)

Submitted to the Program in Media Arts and Sciences,
School of Architecture and Planning,
in partial fulfillment of the requirements for the degree of

Master of Science

at the

MASSACHUSETTS INSTITUTE OF TECHNOLOGY

May 2026

Author_____

Sara Vanessa Fernandez
Program in Media Arts and Sciences
May 15, 2026

Certified by_____

Neil Gershenfeld
Director, MIT Center for Bits and Atoms
Thesis Supervisor

Accepted by_____

Joseph A. Paradiso
Academic Head
Program in Media Arts and Sciences

White-Light Imaging Interferometry

by

Sara Vanessa Fernandez

Submitted to the Program in Media Arts and Sciences,
School of Architecture and Planning,
on May 15, 2026, in partial fulfillment of the
requirements for the degree of
Master of Science

Abstract

Precision metrology is essential to modern science and engineering. Among 3D surface-measurement techniques, white-light interferometry (WLI) is a particularly useful approach because it offers nondestructive nanometer-scale axial resolution of surface features. However, commercially available options are prohibitively expensive. This thesis addresses this gap through the design, construction, and demonstration of a low-cost WLI-based optical profilometer built from a combination of off-the-shelf optical and electronic components, and custom 3D-printed and CNC-milled parts. The system was developed from first principles, with the optical path, mechanical architecture, and computer-controlled scanning designed to satisfy the physical constraints governing WLI. Custom mechanical components, including a flexure and precision lead screw assembly, were designed to enable stable and repeatable motion, while computer-controlled positioning was implemented to translate the sample through the coherence plane in a controlled and reproducible manner. Scan parameters such as scan speed were selected based on optical and sampling considerations required to reliably capture the coherence envelope. Using this approach, a working optical profilometer was realized with a bill of materials of approximately $2.5k and demonstrated axial resolution of 270 nm. The instrument was used to scan several test cases, including a mirror, a step height validation sample, a coin, and a Vickers hardness indentation sample, demonstrating its current 3D surface-scanning capability across targets with different geometries and surface features. Taken together, these results show that high-resolution WLI-based surface metrology can be achieved at a small fraction of the cost of conventional commercial systems, while also establishing a framework for combining physics-based optical design, low-cost fabrication, and computational scanning methods to expand access to precision surface metrology.

Thesis Supervisor: Neil Gershenfeld
Title: Director, MIT Center for Bits and Atoms

White-Light Imaging Interferometry

by

Sara Vanessa Fernandez

The following people served as readers for this thesis:

Thesis Reader_____

Neil Gershenfeld
Director
MIT Center for Bits and Atoms

Thesis Reader_____

Ramesh Raskar
Associate Professor of Media Arts and Sciences
Program in Media Arts and Sciences

Thesis Reader_____

Stephan Schlamminger
Physicist
National Institute of Standards and Technology

Acknowledgements

Thank you to Neil for welcoming me into CBA and for creating a culture of enthusiasm and curiosity around the whole world of making. I have already learned so much from your courses, conversations, and leadership, and I am incredibly grateful for the opportunity to keep learning from you. Thank you also for always bringing real energy to the research, for being so knowledgeable and genuinely excited about new ideas, and for helping set the direction in ways that push us to do cool and meaningful things while making room for free play.

Thank you to my readers, Ramesh and Stephan. Ramesh, thank you for your insights and thoughtful feedback during our sessions together. Stephan, thank you for your support and feedback throughout this process, and for being just as excited as I am about where this project is headed. Thank you also to the National Institute of Standards and Technology (NIST) for supporting this work and for advancing the broader goal of making precision metrology more accessible.

Thank you to everyone at CBA for making my time here as a master's student so meaningful. I have already learned so much from all of you and am incredibly grateful to have found such wonderful friends here. Thank you to my fellow basement-dwellers: Alan, Miana, Eyal, Jiaming, Debu, Ric, Kat, Erik, Camron, Alfonso, Dimitar, Jack, Alex, Quentin, Jake, and surely others who are around in the wee hours. Thank you for helping me find my footing and for helping me grow both as a researcher and as a person. Thank you also to those without whom everything would cease to function: Candace, Kara, Marissa, and

Dan. You are always there to lend an ear or a hand, and you have helped shape CBA into an interesting, supportive culture full of people excited to make things.

Thank you to everyone in MAS who has encouraged me throughout my time here and helped me end up in the best place for me to grow, surrounded by truly exceptional people. Thank you also to my fellow cohort members and friends. Even if it is just a quick coffee chat or a once-in-a-blue-moon dinner together, I am glad we have been there for each other through everything.

Thank you to my friends in DMSE. Thank you to David Bono for always being willing to help and for letting me visit his lab space from time to time. Thank you to Shaymus Hudson for helping with the Vickers hardness tests at The Laboratory for Physical Metallurgy (MetLab) and for having good life advice always at the ready.

Thank you to Leslie and Donzo for making every visit eventful and for bringing much-needed joy whenever you are around. Thank you to Colin for being there for me in more ways than one, and for encouraging me to step completely outside my comfort zone in order to pursue what I truly wanted to do. I am so glad to have you with me. Thank you to Abuela, Da Mommas, Da Pappas, and Da Goose for putting up with my antics and for being so supportive when I show you the exciting new things I've been up to. Thank you to Da Nooch and Nessa for being there for them while I am away. Thank you for occupying my walks to-and-from the lab and for always being willing to talk through anything I'm going through and celebrate wins (on my side and yours). I love you all very much.

Contents

List of Figures

List of Tables

Chapter 1

Introduction

1.1 3D Measurement Techniques

Surface metrology is essential in both research and industry because surface geometry strongly influences device performance, fabrication quality, and process reliability. Accurate topographic measurement is used to quantify surface features, identify defects, assess yield, and refine material processing protocols across a wide range of applications. A variety of techniques are available for this purpose, including non-contact methods such as photogrammetry, structured-light 3D scanning, confocal microscopy, time-of-flight sensing, and white-light interferometry (WLI), as well as contact-based methods such as atomic force microscopy (AFM) and stylus or probe-based measurement. These approaches differ substantially in operating principle, achievable resolution, acquisition speed, measurable area, and system cost, and no single method is optimal across all use cases (Figure 1-1). Accordingly, understanding the strengths and limitations of these methods requires examining the physical mechanism by which each converts optical or mechanical signals into surface height information.

A key distinction between these methods is the physical quantity used to infer depth. Structured-light scanners recover surface height through triangulation, so their depth precision depends on imaging geometry, calibration accuracy, projector pattern quality, camera

resolution, and the tradeoff between field of view and sampling density. As the field of view increases, a fixed number of pixels must cover a larger area, reducing the smallest resolvable feature size unless additional images or higher-resolution hardware are used. Time-of-flight systems instead estimate depth from the travel time or phase delay of reflected light, so their precision is fundamentally limited by timing accuracy and synchronization. Because light travels at approximately $3 * 10^8$ m/s, even picosecond-scale timing errors correspond to sub-millimeter to millimeter-scale distance errors, making these systems well suited to ranging applications but fundamentally less suitable for nanometer- or sub-micrometer-scale surface profilometry. Confocal microscopy provides substantially better axial sectioning than triangulation- or timing-based approaches, but its axial resolution is still governed by diffraction, wavelength, and numerical aperture rather than interferometric phase or coherence localization[1].

Interferometric methods are fundamentally different from triangulation- and time-based techniques because they infer height from the interference of optical fields rather than from macroscopic geometry or light travel time. Their high sensitivity arises from the fact that optical phase changes over distances on the order of the wavelength. However, the coherence of the illumination determines whether this sensitivity can be used to recover absolute surface height unambiguously. In fully coherent, monochromatic interferometry, the measured phase is 2π periodic, so a single phase value can correspond to multiple different surface heights, separated by integer multiples of the wavelength, or by half-wavelength increments in reflection. As a result, although highly coherent interferometry is extremely sensitive to small height changes, it does not by itself provide a unique indicator of absolute surface position over large height variations or discontinuities. Long-coherence illumination is also more susceptible to speckle especially on rough or scattering surfaces[2].

White-light interferometry overcomes these limitations by using a broadband, low-coherence source. Because the coherence length is short, interference occurs only when the optical path lengths in the reference and sample arms are closely matched. During axial scanning, this produces a sharply localized interference envelope at each pixel, and the position of that envelope identifies the surface height. Unlike fully coherent interferometry, low-coherence

interferometry therefore provides additional axial information and enables absolute height determination, even for surfaces containing larger step heights or discontinuities. In this way, WLI preserves the high height sensitivity of interferometry while avoiding the wavelength-period ambiguity that limits fully coherent methods. Fundamentally, this is why WLI can achieve much finer axial resolution than structured-light or time-of-flight methods, since its depth sensitivity is set by interferometric localization and coherence length which allows for absolute positioning, rather than by triangulation geometry or electronic timing precision. In broadband interferometric systems, axial resolution improves as source bandwidth increases because coherence length decreases. This inverse relationship between bandwidth and coherence length is a defining physical advantage of low-coherence interferometry[3].

1.2 Motivation

Lower-resolution techniques such as photogrammetry are commercially available at substantially lower costs than other systems, while higher-resolution methods, such as those based on white-light interferometry and AFM, are correspondingly more expensive, reflecting the expected trade-off between cost and measurement precision. However, measurement requirements in many scientific and engineering applications extend well beyond the capabilities of lower-resolution optical techniques. For many applications, nanometer-scale precision is required; in these cases, contact-based approaches such as AFM, where the probing tip can modify or damage surface features during measurement, may be unsuitable, making non-destructive characterization essential. For resolutions below 10 nm, this constraint largely leaves WLI-based approaches as the practical solution.

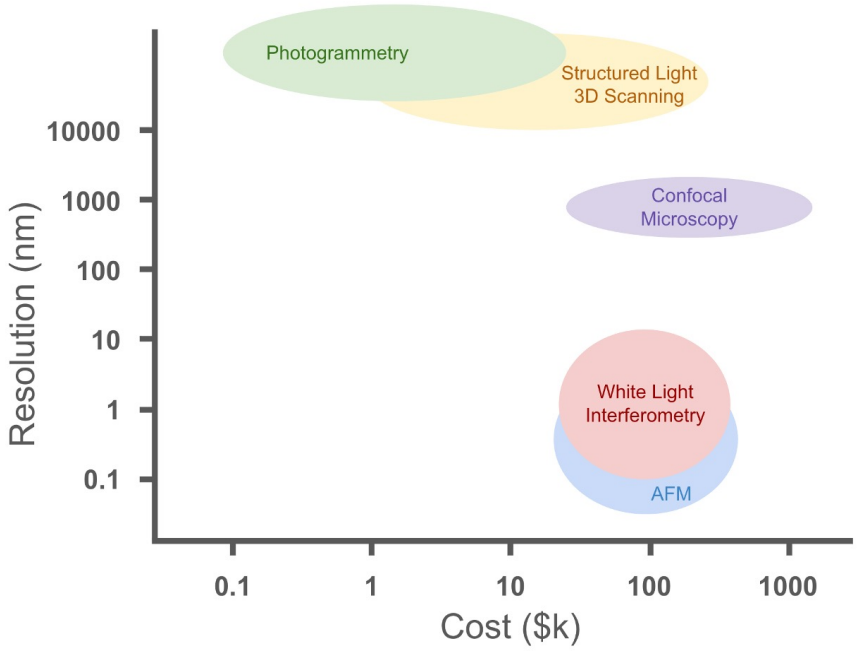

Figure 1-1: Resolution versus cost of commercial surface profiling techniques, including photogrammetry, structured light 3D scanning, confocal microscopy, white light interferometry, and atomic force microscopy.

Despite the usefulness of WLI, these measurement tools remain out of reach for many, with most WLI-based profilometers costing upwards of $100k as can be seen in Figure 1-1. This is largely due to commercial incentives, lack of mass-production, the conventional use of expensive specialized components such as superluminescent diodes (SLEDs), and the advanced software packages that are bundled with these instruments. Additionally, the primary customers of these tools, such as semiconductor manufacturers and large-scale R&D facilities, tend to value throughput far more than low cost. As a result, metrology companies are incentivized to invest in expensive precision motion stages, large-field-of-view imaging sensors, and advanced image-stitching and automation algorithms to achieve faster scan rates tailored to this specific customer base. However, this emphasis overlooks important use cases in settings where high speed and sub-nanometer precision are not essential, such as academic research, emerging startups, and field applications, where lower cost and accessibility are much more valuable.

Key metrics for assessing WLI-based profilometer performance include axial resolution, lat-

eral resolution, field of view (FOV), axial travel range, and scan speed. I have compared the least expensive commercial WLI-based profilometers available[1] using these metrics in Table 1.1. This table was populated based on publicly available datasheets, requested quotes, published pricing, and exchanges with sales representatives. Since these parameters are not consistently defined across products, this table serves as an approximate representation of their performance and cost metrics. The profilometers are included in descending price order, and prices rounded down to the nearest $5k. These products, along with others in the same product line, are priced substantially higher when additional features are included, such as objective lenses that enhance field-of-view and lateral resolution, automation and image stitching options, vibration isolation, higher speed capabilities, and larger stage areas. I have included the least expensive configurations that employ white light interferometry for optical profiling, with the most affordable costing about $40,000. Critically, there are no truly accessible options even at modest performance levels, rendering WLI-based profilometry of any kind exclusive.

[1] I extensively searched for the least expensive WLI-based profilometers available, and there were none priced below $40,000. However, a notable similar tool is Lumedica OQ LabScope, which uses WLI for volumetric scanning of human tissues. Therefore, Lumedica OQ LabScope's resolution is characterized based on its volumetric scanning capability (due to its medical use case in optical coherence tomography for retinal imaging), which is inherently less precise than surface scanning because the peak of the axial point-spread function can be localized more precisely than its width. Although in principle this instrument should be capable of surface scanning when paired with the proper software, I could not find any data to support this, nor specifications on what resolution this would allow it to achieve, so no reliable comparison could be made.

Vendor	Product	Axial Res. (nm)	Lateral Res. (μm)	FOV (mm^2)	Axial Travel (mm)	Scan Speed (μm/s)	Price ($)
Polytec	Pro.Surf – large area optical profiler for quality control[4]	< 1.45	8.4 – 16[a]	44×33; 230×220[b]	70	11.9	150k
KLA	Zeta-20^{TM} Optical Profilometer[5]	13[c]	1.12[d]	0.928×0.776[d]	40	not reported	120k
Bruker	ContourX-100 3D Optical Profilometer[6]	< 0.01	0.13 – 0.38[e]	10×10[f]	≤ 10	37	90 – 120k
Polytec	Metro.Lab – the compact white-light interferometer[7]	< 2.85	29	37×28; 87×78[b]	70	$\sim$ 17–25[g]	85k
MSE Supplies	MSE PRO 3D Optical Surface Profilometer with 220×220 mm Table Size, 1.85 μm/s Scanning Speed[8]	0.1	0.92[d]	0.98×0.98[d]	10	1.85	80k
Polytec	Micro.View – compact 3D surface roughness profiler[9]	0.01	0.59 – 9.76[h]	0.07×0.05; 13.2×9.8[b]	100	100	55k
KLA	Filmetrics Profilm3D Optical Profilometer[10]	not reported	0.92[d]	2.0×1.7[d]	100	12	40k

[a] near-field vs. far-field
[b] with image stitching
[c] reported for motorized stage only
[d] with standard 10X objective
[e] using proprietary AcuityXR® and typical Sparrow criterion, respectively.
[f] for highly specialized 1X lens
[g] extrapolated from 65 nm sampling with 50 micron height variation taking 2-3 seconds
[h] lateral resolution depends on objective used

Table 1.1: Comparison of selected low-cost optical profilometers.

As a result, researchers must travel to expensive centralized facilities or invest in costly proprietary instruments to obtain these valuable measurements, creating logistical bottlenecks that slow iteration. In the absence of nondestructive tools, researchers also resort to destructive workarounds, such as fracturing laser-machined piezoceramics to inspect cross sections for cut depth measurement. This is an inefficient and wasteful substitute for precise, nondestructive inspection.

I have witnessed this very issue during my own previous research and have been told by other researchers that this is also a commonly recurring pain point in their work. Collaborations with NIST have also revealed that a low-cost non-destructive profiling tool would be instrumental in the pursuit of democratizing metrology. If made affordable, such analyses could become routine, which would enable rapid iteration, accelerate development cycles, and offer dependable quality control. The implications span academia and industry, reaching automotive, aerospace, semiconductors, electronics, biology, and medical sectors — all of which depend on reliable surface metrology.

1.3 Prior Art

A limited number of academic groups have explored the development of relatively low-cost non-contact optical imaging systems. I was unable to find any that employed WLI for non-medical imaging. Therefore, the most relevant examples identified in the literature are based on optical coherence tomography (OCT), a low-coherence interferometric imaging modality widely used in medicine. OCT forms depth-resolved images by measuring the interference between light reflected from a sample and light returned from a reference arm, thereby allowing internal structures to be reconstructed with micrometer-scale axial resolution, such as in eye imaging. Because OCT and white-light interferometric (WLI) surface profilometry are both rooted in low-coherence interferometry, these systems provide useful prior art for the present work.

OCT is generally designed for volumetric imaging of partially transparent or scattering samples, especially biological tissue, whereas WLI-based optical profilometry is concerned specifically with accurate reconstruction of the topography of a reflecting surface. As a result, the performance metrics typically reported for OCT systems are not directly equivalent to those used to evaluate a profilometer. In OCT, axial resolution is commonly described by the width of the axial point-spread function or coherence-gated response. For surface metrology, however, the quantity of interest is often the precision with which the axial position of a reflecting interface can be localized. Under favorable conditions, that peak position can be estimated more precisely than the full width of the response. Although OCT-based instruments could in principle be adapted for surface scanning with appropriate optics and reconstruction software, I could not find published demonstrations of their use as dedicated surface profilers, nor reported surface-metrology metrics such as height repeatability, step-height accuracy, or surface reconstruction fidelity. These systems are therefore best understood as related prior art rather than direct precedents.

The closest example identified is a precursor to the commercially available Lumedica OQ LabScope. Kim et al. developed a portable spectral-domain OCT (SD-OCT) system with a reported bill of materials of $7164.[11] Spectral-domain OCT acquires depth information

by measuring the interference spectrum with a spectrometer and reconstructing reflectivity as a function of depth. The system reported by Kim et al. achieved an axial resolution of 7 μm in air, a lateral resolution of 17.6 μm, and an imaging depth of 2.8 mm in air[11]. A commercial descendant of this platform, the Lumedica OQ LabScope, provides a useful additional reference point because it represents the translation of a low-cost academic OCT concept into an available instrument. The base model is reported to offer an axial resolution of 8 μm, a lateral resolution of 18 μm, and a field of view of 5×5 mm^2[12]. While this demonstrates that compact OCT systems can achieve strong performance at substantially lower cost than many conventional optical instruments, it remains a biomedical imaging platform rather than a dedicated profilometer.

Another recent academic example is the compact OCT system reported by Wang et al., with an approximate bill of materials of \$5000.[13] This work further reinforces the broader trend that OCT hardware costs can be reduced substantially through careful system design and component selection. However, as with the examples above, the instrument was developed as an OCT imaging system rather than as a surface metrology tool, and the reported performance metrics are therefore not directly comparable to those used in profilometry. The most relevant examples are summarized in Table 1.2. Reported specifications are reproduced from the cited sources.

System	**Price (\$)**	**Axial Res. (μm)**	**Lateral Res. (μm)**	**Axial Range / Depth (mm)**	**FOV (mm^2)**
Portable OCT precursor to the Lumedica OQ LabScope[11]	7164 BOM	7	17.6	2.8	not reported
OQ LabScope 3.0[12]	$>$ 12,495	8[a]	18[a]	not reported[b]	5×5[a]
Compact low-cost OCT system[13]	5000 BOM	not reported	not reported	not reported	not reported

[a] reported for the base commercial OQ LabScope configuration in the cited specification materials
[b] publication reports imaging depth of a few millimeters, but manufacturer product page does not

Table 1.2: Representative low-cost OCT systems developed in academia.

Taken together, these examples establish an important benchmark, showing that low-coherence interferometric imaging systems can be built at costs far below those of many commercial optical instruments while still maintaining useful imaging performance. At the same time, they highlight a clear gap in the literature: low-cost OCT systems have largely been developed for volumetric biomedical imaging rather than for high-precision

non-contact surface profilometry. The present work addresses this gap by lowering the cost of white-light interferometric profilometry while preserving high imaging resolution, thereby extending this class of instrument into a previously underserved region to the left of the WLI bubble in Figure 1-1.

Chapter 2

Background and Theory

2.1 White-Light Interferometry

White-light interferometry (WLI), also known as coherence scanning interferometry, is a non-contact optical metrology technique for three-dimensional surface profiling. It uses broadband light and interference-based measurement to characterize surface topography with nanometer-scale axial precision, enabling measurement of features such as micron-scale height variations, roughness, and step heights without physically contacting or otherwise damaging the sample.

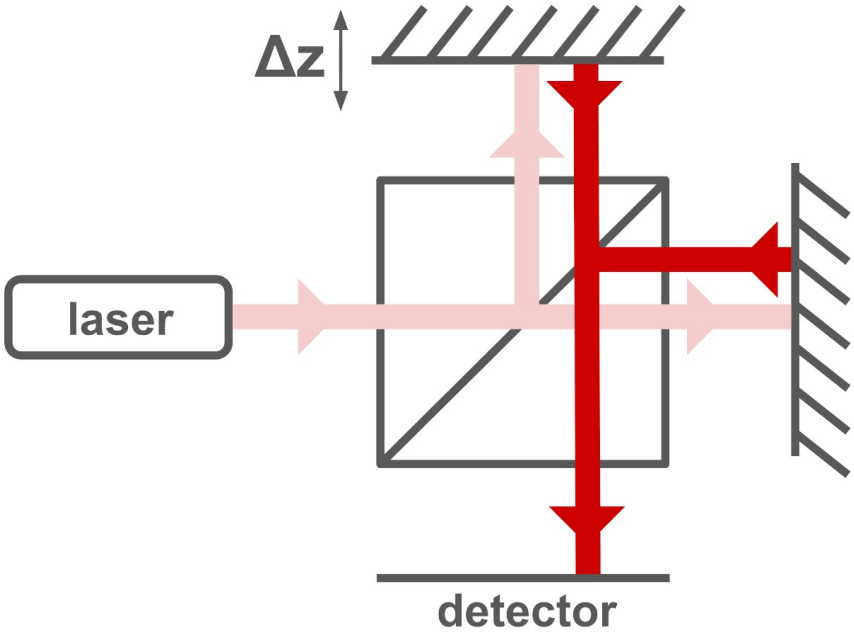

Figure 2-1: Michelson setup.

In a typical Michelson interferometry setup such as is depicted in 2-1, light from a source is split into a reference arm and a sample arm, reflected back from each, and then recombined to produce an interference signal. In WLI, the source has low temporal coherence, so interference is only observed when the optical path lengths of the reference and sample arms are nearly matched. This localization of the interference signal enables precise identification of surface position along the optical axis and subsequent reconstruction of the surface topography. This is because light with low temporal coherence is non-periodic and localizes the interference signal near the position where the reference and sample beams have traveled the same effective optical distance, allowing axial surface position to be unambiguously identified. Conversely, highly temporally coherent light produces interference over a long axial range, yielding a periodic signal in which similar fringe patterns recur at multiple axial positions, making the true surface location ambiguous.

White-light interferometry therefore requires a light source that is broadband, and thus low in temporal coherence, while still having sufficient spatial coherence to produce stable interference. Spatial coherence and temporal coherence are orthogonal measures of how well the wave can be predicted at a single point in space or time, respectively, whereby

spatial coherence describes lateral correlations across a wavefront and temporal coherence describes axial correlations along the direction of propagation.

2.1.1 Spatial Coherence

For the purposes of this work, spatially coherent light can be described as originating from a single diffraction-limited point in space based on the divergence angle. An illumination source that emerges from a diffraction-limited spot will necessarily take on a wide Gaussian distribution in the far field because Fourier optics specifies that the far field beam pattern is the Fourier transform of the source, whereby the diffraction limit dictates that the spot size is at least half the illumination wavelength in diameter. The numerical aperture can be used to calculate the divergence angle, and this in combination with the illumination wavelength reveals the spot size, which sets the dimensions of the diffraction-limited point in space. If the light is emitted just from that point with that divergence angle, then it is, by definition, spatially coherent.

2.1.2 Temporal Coherence and Spectral Bandwidth

Temporal coherence describes the correlation of the optical field at a single point over time and is closely tied to the source bandwidth, where broader spectral bandwidth corresponds to shorter temporal coherence length. In WLI, the illumination source should be broadband enough to provide short temporal coherence while retaining sufficient spatial coherence to form high-contrast interference fringes across the sample region of interest. Mathematically, this relationship arises because the temporal coherence function in the time domain and the source spectrum in the frequency domain form a Fourier transform pair. As a result, a source with a broader spectrum has a narrower coherence function and therefore a shorter coherence length. The following equations make this relationship explicit[14].

For a source with frequency bandwidth $\Delta\nu$, the coherence time scales as

$$\tau_c \sim \frac{1}{\Delta\nu}, \tag{2.1}$$

where τ_c is the coherence time.

The coherence length in a medium of refractive index n is then

$$L_c = \frac{c}{n}\tau_c \sim \frac{c}{n\Delta\nu}, \tag{2.2}$$

where L_c is the coherence length and c is the speed of light in vacuum.

To rewrite this in terms of wavelength, use

$$\nu = \frac{c}{\lambda}, \tag{2.3}$$

where λ is the vacuum wavelength. Differentiating gives

$$d\nu = -\frac{c}{\lambda^2}\, d\lambda. \tag{2.4}$$

Approximating over a narrow bandwidth about the central wavelength λ_0 gives

$$\Delta\nu \approx \frac{c}{\lambda_0^2}\Delta\lambda, \tag{2.5}$$

where $\Delta\lambda$ is the wavelength bandwidth and λ_0 is the central wavelength.

Substituting into the expression for coherence length gives

$$L_c \sim \frac{c}{n\Delta\nu} \sim \frac{c}{n(c/\lambda_0^2)\Delta\lambda} = \frac{\lambda_0^2}{n\Delta\lambda}. \tag{2.6}$$

Thus,

$$L_c \sim \frac{\lambda_0^2}{n\Delta\lambda}. \tag{2.7}$$

In Michelson white-light interferometry, the optical path difference changes by twice the physical displacement since the light traverses the measured path twice. Therefore, if L_c is expressed as a one-way physical displacement,

$$\boxed{L_c \sim \frac{\lambda_0^2}{2n\Delta\lambda}} \tag{2.8}$$

This derivation is intended as an approximation that captures the dominant scaling of coherence length with source bandwidth. It assumes a Gaussian source spectrum, for which the temporal coherence function is likewise Gaussian because the two are Fourier-transform pairs. Real broadband sources, however, are not perfectly Gaussian and often contain additional spectral structure, which can produce sidelobes in the coherence envelope and contribute to ghost coherence planes. A more rigorous treatment would use wavenumber rather than wavelength, since optical path difference varies linearly with wavenumber but nonlinearly with wavelength over broad bandwidths. Even so, for the present source and bandwidth, the Gaussian wavelength-based approximation provides a reasonable estimate of the characteristic coherence length.

In the classical definition of resolution, coherence length relates to axial resolution according to the separability of two reflectors in the axial direction. In that case, the axial resolution would be half of the FWHM. In this work, the coherence length was determined empirically rather than analytically, since the source spectral bandwidth required for the calculation was not known and the coherence length could be measured directly to be 9.57 um using the FWHM definition, thereby avoiding errors introduced by approximation[15], making the axial resolution according to the separability of two reflectors in the axial direction about 4.785 um. However, for a surface measurement which is a sparse single-point measurement, there is no separability problem but instead a peak-finding problem, which can be solved more accurately yielding the higher axial resolution of 270 nm.

2.1.3 Scattering Angles and Efficiency

The amount of light collected from a sample depends on both the angular distribution of the scattered light and the numerical aperture (NA) of the objective lens. As an idealized model for a diffusely scattering surface, the sample can be treated as Lambertian, meaning

that the radiant intensity varies with scattering angle θ according to Lambert's cosine law:

$$I(\theta) = I_0 \cos\theta \tag{2.9}$$

where θ is measured from the surface normal and I_0 is the intensity in the normal direction.

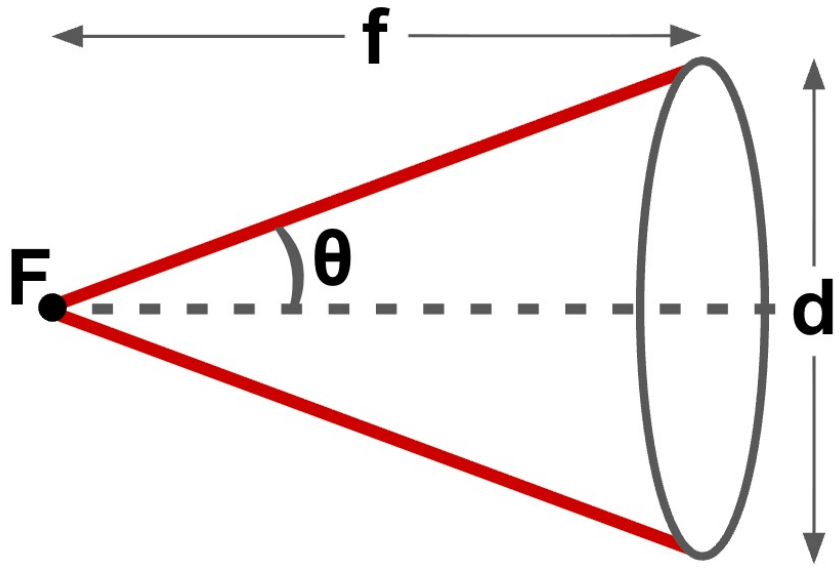

Figure 2-2: Numerical aperture diagram. F is the focal point, f is the focal distance, d is the diameter of the lens, and θ is the collection angle.

This is the Abbe diffraction limit which defines the spot size:

$$r_{\text{spot}} = \frac{\lambda}{2\,\text{NA}} \tag{2.10}$$

where r_{spot} is the radius of the spot in meters, λ is the wavelength of light in meters, and NA is the numerical aperture of the lens.

Referring to Figure 2-2, an objective lens collects only the light scattered within its acceptance cone, defined by the maximum collection angle θ. The numerical aperture is related to this angle by

$$\text{NA} = n\sin(\theta), \tag{2.11}$$

where n is the refractive index of the medium between the sample and the objective. From

geometry, the appropriate NA can be calculated from the focal length and diameter of the lens as follows.

$$tan(\theta) = \frac{d}{2f} \tag{2.12}$$

$$\mathrm{NA} = n\frac{d/2}{\sqrt{f^2 + (d/2)^2}} \tag{2.13}$$

For a Lambertian surface, the collected fraction of the diffusely scattered power is found by integrating the angular power distribution over the solid angle accepted by the objective and normalizing by the total scattered power over the hemisphere:

$$\eta = \frac{\displaystyle\int_0^{2\pi}\int_0^{\theta_{\max}} I_0 \cos\theta \sin\theta \, d\theta \, d\phi}{\displaystyle\int_0^{2\pi}\int_0^{\pi/2} I_0 \cos\theta \sin\theta \, d\theta \, d\phi}. \tag{2.14}$$

Evaluating the integrals gives

$$\eta = \sin^2\theta_{\max}. \tag{2.15}$$

Substituting the definition of numerical aperture yields

$$\eta = \left(\frac{\mathrm{NA}}{n}\right)^2. \tag{2.16}$$

Thus, for an ideal Lambertian scatterer, the collection efficiency scales with the square of the normalized numerical aperture. In air, where $n \approx 1$, this reduces to

$$\boxed{\eta \approx \mathrm{NA}^2} \tag{2.17}$$

The degree to which polarization is preserved after light is reflected off a Lambertian surface also contributes to optical power loss and efficiency determination. In the ideal Lambertian limit, the diffusely reflected component is typically treated as depolarized, so the fraction of the incident polarization state that is preserved is approximately zero:

$$P_{\text{preserved}} \approx 0. \tag{2.18}$$

Equivalently, if the illumination is linearly polarized and the detection path selects only the original polarization state, the diffuse Lambertian component contributes, on average, only half of its power:

$$\eta_{\text{pol}} \approx \frac{1}{2}. \tag{2.19}$$

Accordingly, the collected power transmitted through a polarization-selective detection path may be approximated as

$$\eta_{\text{total}} \approx \eta\,\eta_{\text{pol}} = \frac{1}{2}\left(\frac{\text{NA}}{n}\right)^2. \tag{2.20}$$

This means that the surface roughness of the sample will affect the effective attenuation in the form of a depolarization coefficient ranging from 0.5 to 1. This will be further explored below in relation to optical power reaching the camera.

Chapter 3

Optical Design

3.1 Light Source

White-light interferometry (WLI) requires a broadband (i.e., low temporal coherence) light source to enable high precision measurement. With a short coherence length, interference will only occur when the two optical paths are matched very precisely, making them capable of achieving higher resolution. WLI also requires high spatial coherence such that light from the reference and sample arms remain phase-correlated across the objective aperture, allowing stable interference fringes to form.

3.1.1 Conventional Approach

Conventionally, WLI has been implemented using superluminescent diodes (SLDs), edge-emitting semiconductor light sources that operate via superluminescence. SLDs deliver high optical power and high spatial brightness similar to that of a laser, while maintaining a broad bandwidth (i.e., short temporal coherence) like an LED. However, SLDs cost several thousands of dollars, with the most common butterfly package selling for around $5,000[16] and the most inexpensive individual SLDs listed at $864.52 with an associated lead time[17]. Thorlabs also offers a Laser-Pumped Phosphor Broadband Light Source for around

$12,500[18] that can be used in WLI systems. In order to develop a low-cost WLI system, an alternative high power density light source was required.

3.1.2 LED

Since LEDs are broadband and readily available at low cost, I initially investigated high-brightness LEDs with compact emission regions as potential illumination sources. To this end, I purchased red[19], blue[20], and white[21] LEDs from ams-OSRAM and designed custom driver boards for each in KiCAD. The boards were made mechanically compatible with optical cage and rod hardware to facilitate future integration into the profilometer setup. After milling and testing the boards in-house, I ordered aluminum-core versions from JLCPCB so that the board itself could also serve as a heat sink.

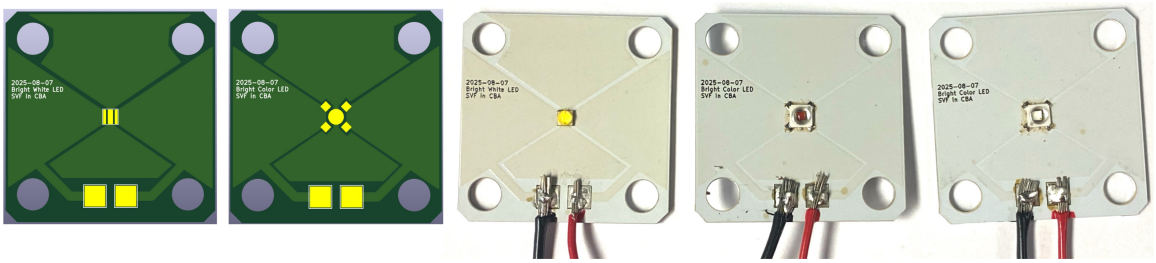

Figure 3-1: Designed and assembled bright LED boards.

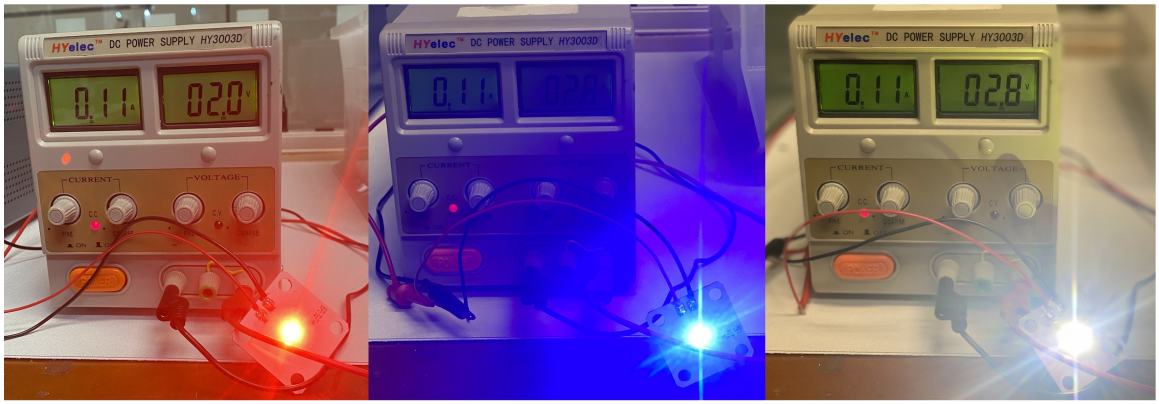

Figure 3-2: Bright LEDs on at 0.11 A, where red and blue are rated for 1.5 A and white is rated for 1.8 A.

Figure 3-2 shows the assembled LEDs operating at just under 10% of their maximum

rated currents. I then assembled a test setup including a heat sink, optical rods, and a collimating optic to evaluate the source. A thermocouple and FLIR camera were used to confirm that the thermal load remained within reasonable limits, even after operating at maximum brightness for ten minutes. Note that the light was not properly collimated for the thermal test.

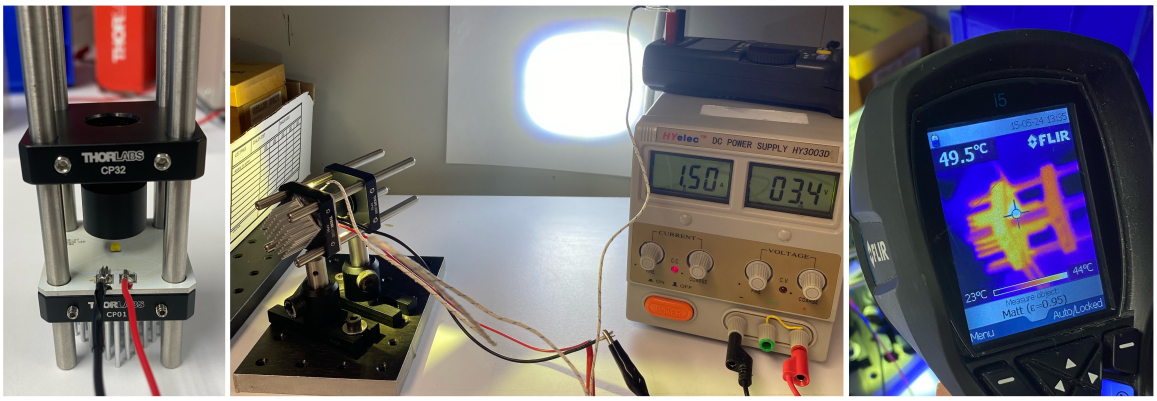

Figure 3-3: Thermal testing setup for the bright LED source.

The LED source was also incorporated into the WLI-based optical profilometer under development at the time. Although the source appeared bright to the naked eye, the illumination at the sample was insufficient to produce the fringe contrast needed for high-frame-rate scanning.

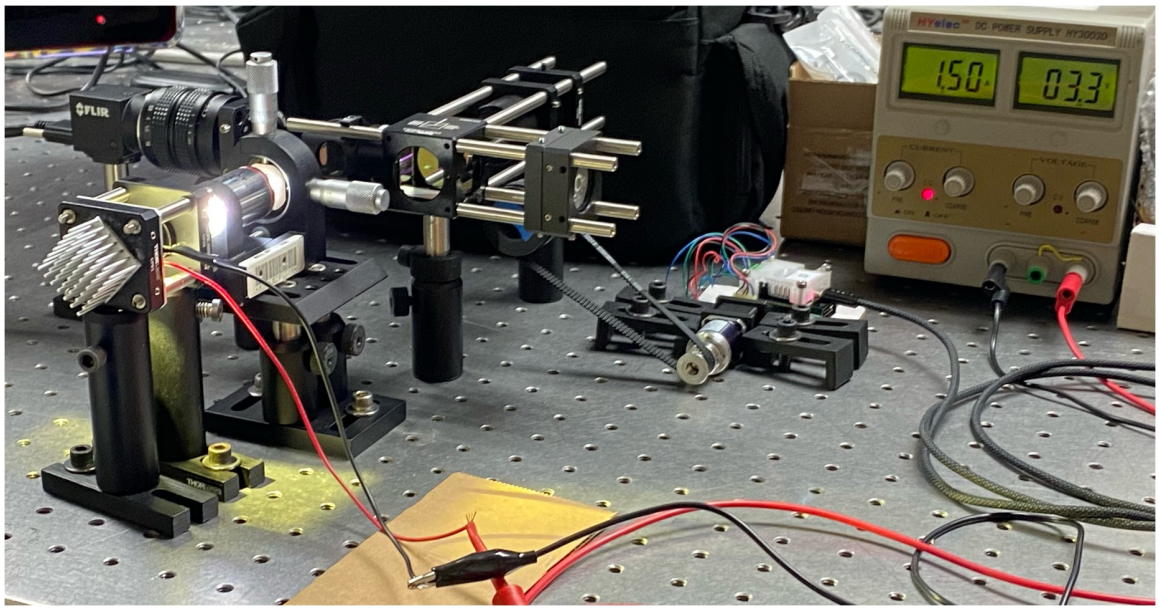

Figure 3-4: Bright LED integrated into the optical setup.

This limitation arises because a conventional LED does not provide sufficient radiance (i.e., power density) for efficient coupling through the very small pinhole required for interferometric imaging. As an order-of-magnitude estimate, consider an LED with emitting area on the order of

$$A_{\text{die}} \sim 1 \text{ mm}^2, \tag{3.1}$$

and optical output on the order of

$$P_{\text{opt}} \sim 1 \text{ W}. \tag{3.2}$$

The corresponding average optical power density at the emitting surface is then

$$\frac{P_{\text{opt}}}{A_{\text{die}}} \sim \frac{1 \text{ W}}{1 \text{ mm}^2} = 1 \ \mu\text{W}/\mu\text{m}^2. \tag{3.3}$$

For a pinhole of diameter 5 μm, as used in this work, the pinhole area is

$$A_{\text{ph}} = \pi(2.5 \ \mu\text{m})^2 \approx 19.6 \ \mu\text{m}^2. \tag{3.4}$$

Scaling only by area gives

$$P_{\text{ph}} \sim \left(1\ \mu\text{W}/\mu\text{m}^2\right)\left(19.6\ \mu\text{m}^2\right) \approx 20\ \mu\text{W}, \tag{3.5}$$

which is the upper limit imposed by the conservation of etendue. Therefore, while these LEDs are visually bright, conventional large-area LED emitters do not provide sufficient power density to deliver useful optical power through such a small pinhole.

3.1.3 Sub-Threshold Laser Diode

Unlike LEDs, laser diodes have very small emitting regions and therefore much higher power density, making them far better suited for focusing light through a small pinhole and delivering sufficient illumination to a sample. This is because lasers amplify light within an elongated waveguide and then emit from a small edge region, often referred to as a facet, which gives them higher power density and higher spatial coherence due to the smaller size as compared to an LED[22]. In addition, the high spatial coherence of a laser makes the coherence plane much easier to locate during alignment than when using an LED, whose very low spatial coherence makes this more difficult.

However, a laser operated above the lasing threshold is too coherent for WLI-based low-temporal-coherence measurements. LEDs naturally provide low temporal coherence because they emit via spontaneous emission over a broad spectral bandwidth, whereas lasers above threshold emit via stimulated emission and therefore produce highly coherent, narrowband, and well-collimated light. To use a laser diode as a low-coherence source, it must therefore be operated below its lasing threshold, where spontaneous-emission-dominated output broadens the spectrum and reduces coherence.

For the 650 nm, 5 mW laser diode used in this work, the lasing threshold occurs at approximately 9.5 mA. Therefore, the diode was driven below this threshold (eventually settling on a value of 8.8 mA) so that it could serve as a lower-coherence illumination source while still retaining the key advantage of a very small emitting area. This combination of reduced coherence and high power density makes a sub-threshold laser diode a more practical source

than a conventional LED for coupling light through the pinhole and achieving sufficient sample illumination.

To adapt the laser source for use in a low-temporal-coherence and high-spatial-coherence application, its spatial coherence should be improved. Although lasers are inherently highly coherent, they can also exhibit residual spatial structure and well-defined transverse modes that are undesirable because they can introduce speckle, nonuniform illumination, and source-dependent artifacts into the measurement. In theory, a multi-mode laser could be used, but the extreme alignment precision required makes this largely impractical. A pinhole spatial filter can therefore be employed to suppress higher-order spatial modes and remove high spatial frequency components, yielding a smoother and more uniform beam profile. The fewer spatial modes pass through the pinhole, the easier alignment becomes. Also, the smaller the emission region, the larger the divergence angle, which allows for a larger field of view for the camera due to the larger equally-illuminated region.

For most laser diodes operating below the lasing threshold, the spectral bandwidth can be expressed as a percentage of the center wavelength, so short wavelengths tend to have smaller absolute bandwidth compared to longer wavelength diodes. To achieve larger absolute bandwidths, long wavelengths are generally preferred. Therefore in addition to the red diode laser used in this work being conveniently available, it is also a good choice for this reason. An exception to this is some green laser diodes which exhibit larger bandwidths due to alloy disorder in materials like InGaN and may be worth exploring in future.

3.1.4 Laser Power Supply

In order to minimize current fluctuations and keep the laser power as stable as possible, I designed a laser power supply board to replace the off-the-shelf power supply that had been powering the laser. I used an LT3080 which is a low dropout linear regulator capable of acting as a precision, low noise current source, listed as 40 µVRMS wideband (10 kHz to 100 kHz) from Digikey[23].

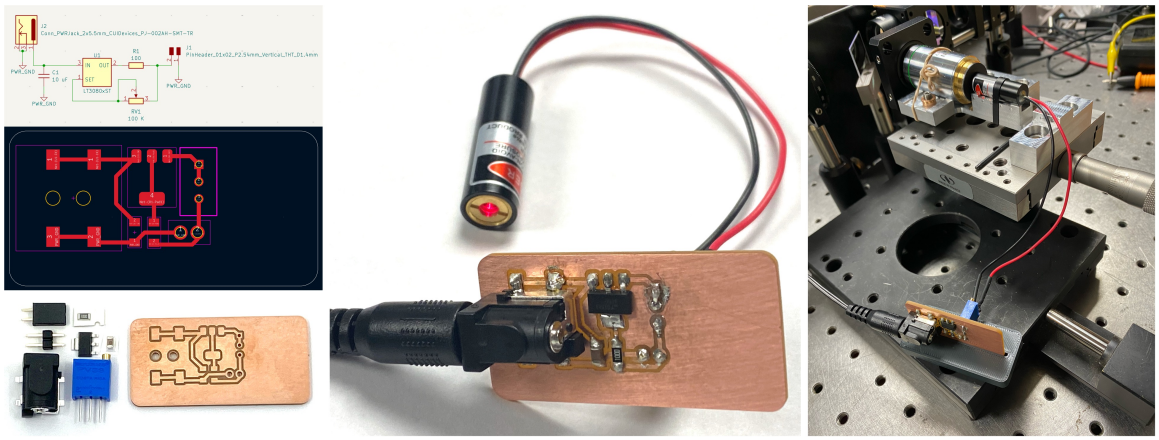

Figure 3-5: Laser power supply design, assembly, and integration into the spatial filter.

The current source was set to 8.8 mA, which is below the approximate lasing threshhold of 9.5 mA, by measuring the in-line current while turning the potentiometer. Without this board, using a benchtop power supply directly sometimes caused visible flickering of the light source which added noise and instability to the optical signal. With it, the current and resulting beam are stable. An output capacitor can be added to further reduce noise coming from the regulator as is typically best practice for low-noise power supplies, but for this particular application where current is intentionally kept constant, the effects of this would be negligible. The board is mounted in a custom 3D-printed PETG stand to prevent shorts with the metal stage it rests upon.

3.2 Illumination Path

3.2.1 Overview

The WLI-based optical profilometer designed and built in this work (Figure 3-6) contains an illumination path followed by a return path (Figure 3-7). The illumination path begins at the sub-threshold laser diode set to a constant 8.8 mA by the laser power supply. The collimated light then exits the sub-threshold laser diode and passes through the 20X objective lens (NA of 0.40), which focuses it onto the 5um pinhole. The beam then diverges from the pinhole and hits the 50:50 epi-illumination beamsplitter plate, which reflects 50%

of the light towards the achromatic doublet mounted onto the 50:50 polarizing beamsplitter cube. When the light hits the achromatic doublet one focal distance away from the pinhole (specified to be 80 mm), the light becomes collimated and continues to travel towards the polarizing beamsplitter cube. The polarizing beamsplitter cube, as the name suggests, splits the beam into two orthogonal polarizations, with 50% of the light transmitting through it towards the reference mirror with one polarization. The remaining 50% of the light is reflected at 90° with the opposite polarization towards the sample surface.

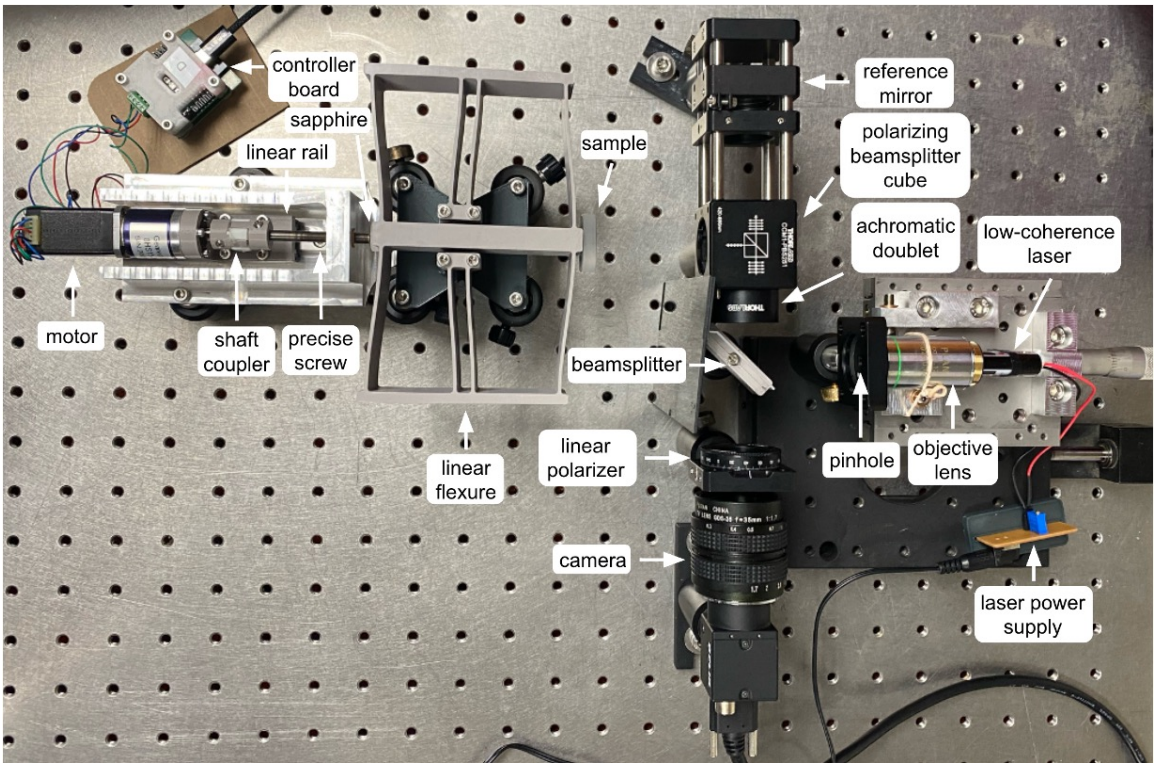

Figure 3-6: System overview.

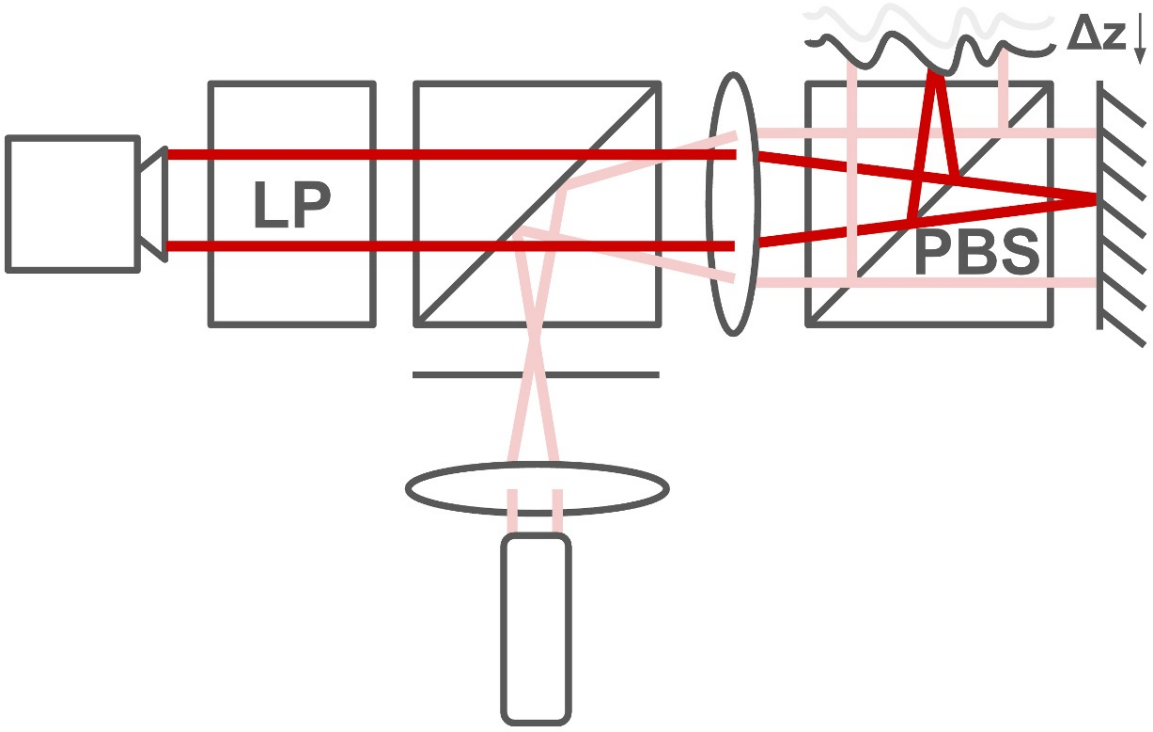

Figure 3-7: Illumination (light red) and return (dark red) paths.

3.2.2 Spatial Filter

A collimated broadband source can be passed through a spatial filter to block higher-order spatial modes, reject scattered light, and subsequently transmit a more uniform, highly spatially coherent beam. A spatial filter typically consists of a focusing optic, a pinhole positioned at the focal plane, and a collimating optic. Together, these elements transmit the central, well-focused portion of the field while blocking unwanted spatial components, resulting in a smoother beam profile that more closely approximates an ideal Gaussian distribution. In interferometric imaging, this improved beam quality promotes more uniform illumination and more stable, high-contrast fringe formation at the expense of optical throughput, since part of the incident light is intentionally blocked by the pinhole.

To balance beam quality against optical throughput, the pinhole diameter must be chosen carefully. If the pinhole is too small, the beam is excessively clipped, increasing diffraction and power loss. This reduces sample illumination and the resulting light available to the

camera, limiting achievable frame rates and potentially requiring higher gain, which introduces noise. If the pinhole is too large, though, unwanted spatial structure is transmitted and the filtering effect is weakened, reducing fringe contrast and therefore limiting measurement resolution. A common design approach is to select the pinhole diameter based on the diffraction-limited spot formed by the focusing optic, then choose a practical diameter approximately 30% larger to avoid excessive clipping while still providing effective spatial filtering[17]. The following calculations quantify this tradeoff and justify the pinhole size used in the present system.

Since the beam did not fill the full pupil of the nominal 20× objective, the beam diameter at the pupil was measured empirically to be 3.33 mm, compared to an effective pupil diameter of 9 mm. The effective numerical aperture was therefore estimated by scaling the nominal objective numerical aperture by the ratio of the beam diameter to the pupil diameter:

$$\mathrm{NA}_{\mathrm{eff}} = \mathrm{NA}_{20\times}\left(\frac{d_{\mathrm{beam}}}{d_{\mathrm{pupil}}}\right) = 0.40\left(\frac{3.33}{9}\right) = 0.148. \tag{3.6}$$

Using $\lambda = 650$ nm, Equation (2.10) then gives

$$r_{\mathrm{spot}} = \frac{0.650\ \mu\mathrm{m}}{2(0.148)} = 2.20\ \mu\mathrm{m}. \tag{3.7}$$

This corresponds to a spot diameter of

$$d_{\mathrm{spot}} = 2r_{\mathrm{spot}} = 4.39\ \mu\mathrm{m}. \tag{3.8}$$

A common practical guideline is to choose the pinhole diameter to be somewhat larger than the diffraction-limited spot in order to avoid excessive clipping. Using a factor of 1.3, the estimated pinhole diameter becomes

$$d_{\mathrm{pinhole,est}} \approx 1.3\, d_{\mathrm{spot}} = 1.3(4.39\ \mu\mathrm{m}) = 5.71\ \mu\mathrm{m}. \tag{3.9}$$

The pinhole used in the present system had diameter

$$d_{\text{pinhole}} = 5\ \mu\text{m}. \tag{3.10}$$

Thus, the chosen pinhole was slightly smaller than the 1.3× estimate, but still very close to the diffraction-limited spot diameter itself. Since the minimum pinhole diameter required to pass the full focused spot without clipping is approximately 4.39 μm, the 5 μm pinhole should still transmit essentially all of the central lobe while providing effective spatial filtering.

Precise alignment is challenging but necessary, and the better the alignment is, the greater power density can pass through the pinhole and the greater illumination the reference mirror and sample receive. This allows for higher frame rates and less gain which makes the mechanical scanning of the sample through the coherence plane faster and less noisy. Ideally, the light will maximally diverge from the pinhole such that it can maximally illuminate the sample, so it should be positioned as close to the achromatic doublet's focal plane as possible.

The spatial filter that I initially used (Figure 3-8) was a commercial off-the-shelf option already in our lab that I combined with various mismatched mounting components to achieve proper alignment. However, that model is no longer manufactured, it is not compatible with a laser diode illumination source, and modern pinholes are not compatible with its magnetic mounting method.

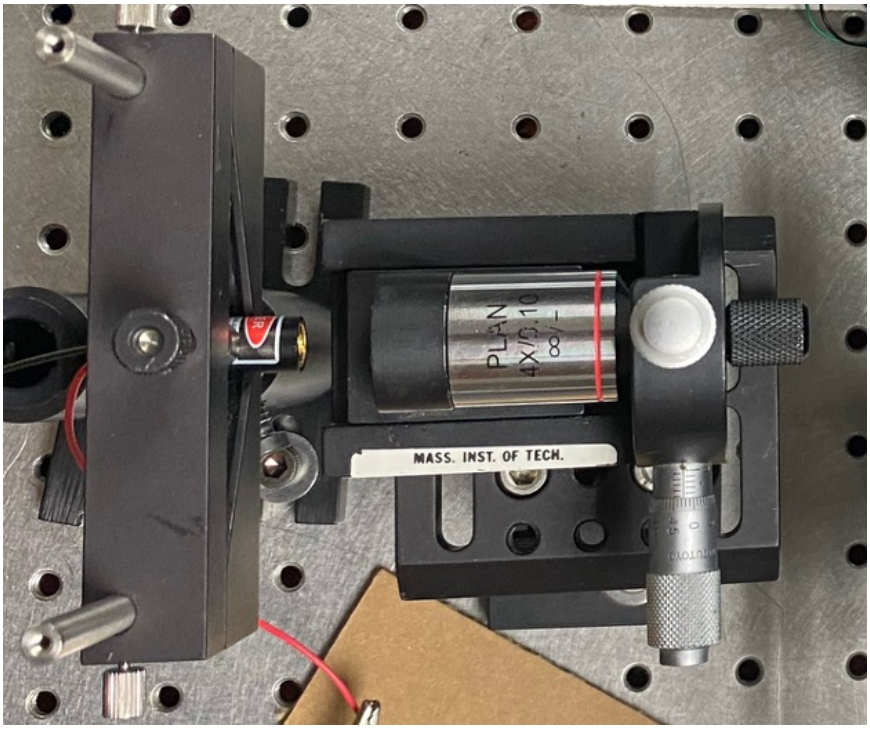

Figure 3-8: Old spatial filter.

Therefore, I designed a two-part portion of a spatial filter out of aluminum that accounted for these needs. The first part was designed to support both the laser diode module and the objective lens. It was designed to mount onto an off-the-shelf linear translation stage. Countersunk holes for 1/4"-20 screws to pass through were added. The contact points designed for both the laser diode module and the objective lens were chamfered for more stable and reliable positioning of these two optical components.

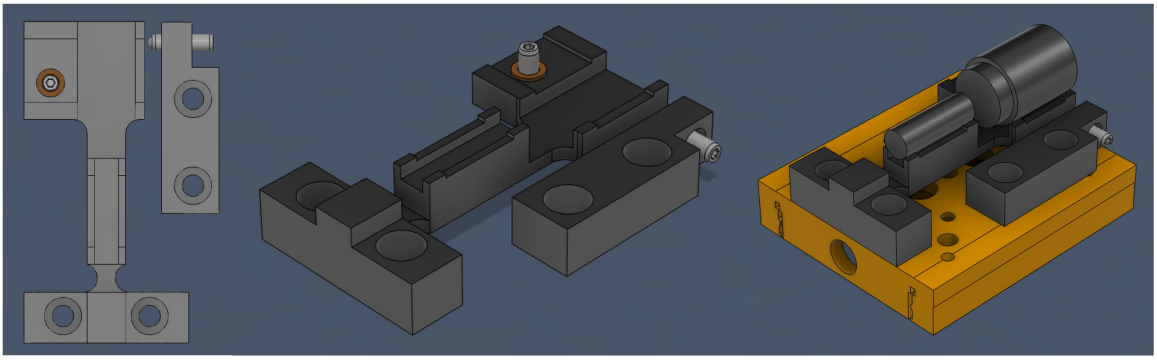

Figure 3-9: Spatial filter CAD.

To have precision position control along the x- and y-axes, a flexural beam was designed which could be bent in the x- and y-directions in response to an applied force. For these adjustments to be possible, the beam closest to the screw holes was made to be thin in the x- and z-directions. This design is capable of deforming by several millimeters in either direction, making effective use of its two degrees of freedom.

To control this deformation precisely, precision hex adjuster screws of $\frac{1}{100}$ inch pitch were selected to enact the pushing force on each of the two flexing directions, respectively. Each of the two parts of the spatial filter were designed with a hole to accommodate a threaded bushing.

After completing the CAD, generating the CAM, and going through the simulation in Fusion, I clamped the aluminum block into the machine with help from Dan and Colin, probed the three orthogonal surfaces about a corner, and CNC machined the parts. For the armature part that supports the laser diode module and the objective lens, I performed 3-axis machining with two setups. For the pusher part that houses the bushing and precision hex adjuster that pushes on the other part in the x-direction, two setups were used.

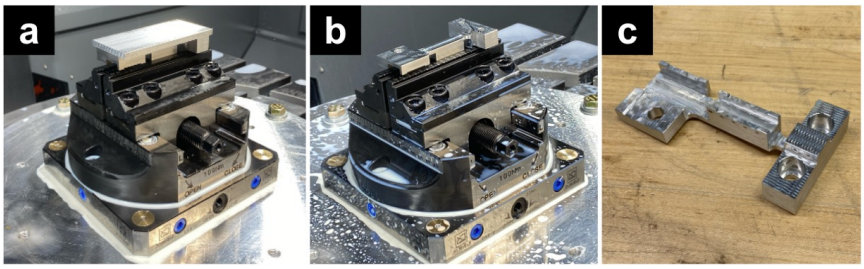

Figure 3-10: Armature machining showing (a) second setup before machining in first setup and (b) after machining with (c) the resulting armature.

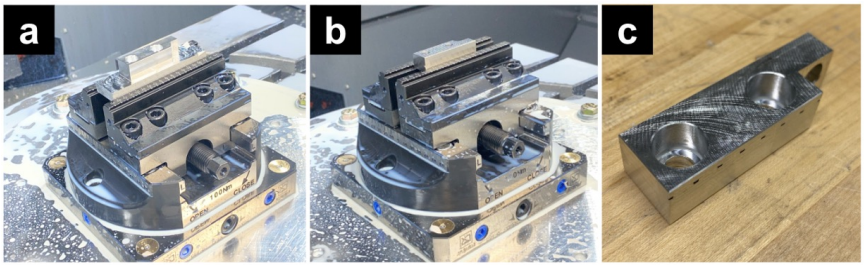

Figure 3-11: Pusher machining showing (a) first setup after machining, (b) second setup after machining, and (c) the resulting pusher.

Once completed, I tested the flexure behaved as expected by screwing it to the optical table and applying an arbitrary force in the x-direction followed by the y-direction and recording this with a microscope. The flexure was indeed able to flex across several millimeters.

After machining the parts, I covered the ends of the two bushings with tape, sanded them, removed the tape, and adhered the two bushings into their respective holes using a minimal quantity of Gorilla glue so as to avoid contaminating the screw threads with the glue. IPA can be used to soften the glue once it cures so that it can be removed, but doing so risks removing the lubricant the screw threads are prepared with.

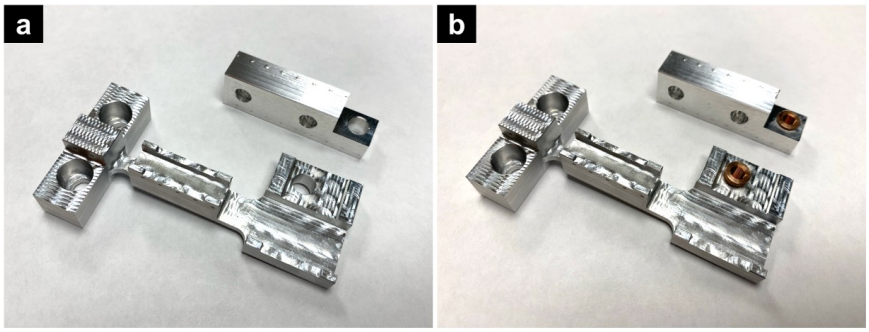

Figure 3-12: Adding bushings.

I then assembled the spatial filter, screwing the aluminum parts onto posts mounted on the linear translation stage. I added the laser diode module and objective lens in their respective mounts and looped rubber bands around them to secure them to the aluminum in a low-cost way. The 20X objective lens included in part c of Figure 3-13 was what was ultimately used in the setup due to its higher NA compared to that of the 4X objective lens in part b of Figure 3-13.

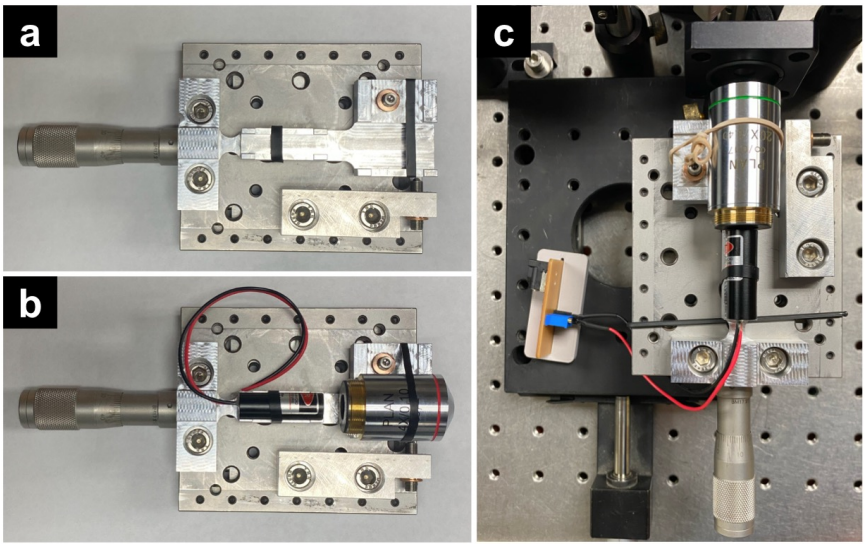

Figure 3-13: Spatial filter assembly.

Initially, the steel ball-tipped precision hex adjuster pushed directly on the aluminum surface, but I quickly realized that this was causing a small mark to be carved into the side of the aluminum part. In response to this realization, I cut a glass slide and added it to the side of the aluminum part to act as the contact point for the adjuster.

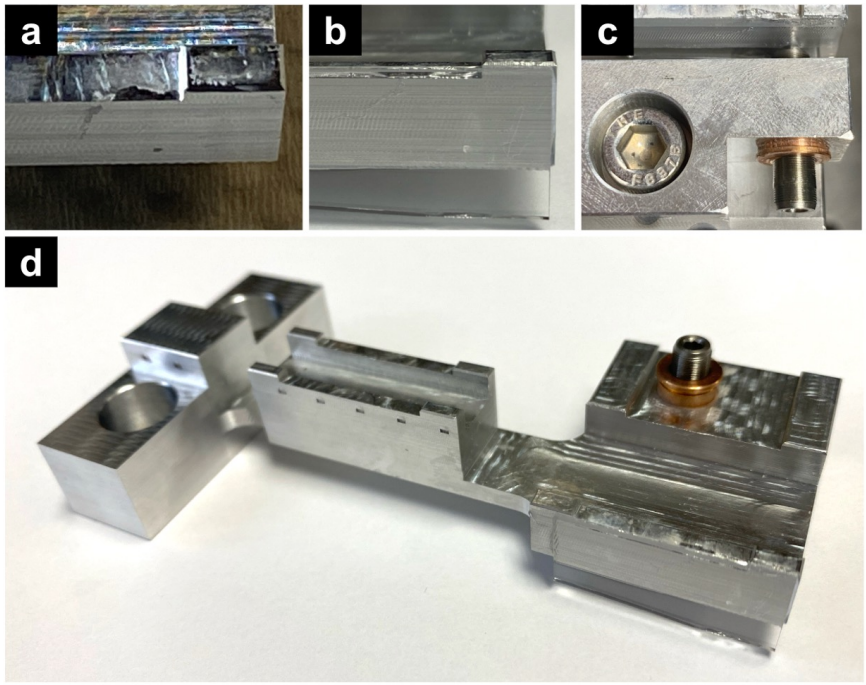

Figure 3-14: Glass interface in spatial filter armature. (a) Mark carved into aluminum, (b) replacement glass interface, (c) glass interface in situ, and (d) modified spatial filter armature.

It was important to ensure that the glass slide extended beyond the bottom surface of the aluminum part because the glass position shifts upwards along with the aluminum in response to positive y-axis adjustments. At first, I neglected to account for this and ended up chipping off pieces of glass when the adjuster applied force at the glass's edge. To remove the first one, I added some IPA to the aluminum-glass interface, applied a bit of prying force, and it came right off. To align the beam, I needed to align it in the x- and y-direction with the pinhole and also needed to position the objective lens one focal distance away from the pinhole. I aligned the beam using a precision hex adjuster by turning it with an Allen key and used the off-the-shelf linear translation stage to adjust the z-position.

3.2.3 Pinhole

To align the pinhole with respect to the lens that follows it, I shone a laser from where the sample was positioned through the polarizing beamsplitter cube and adjusted the an-

gle of the beamsplitter plate until the beam was centered and filled the camera's field of view. Then, I positioned the pinhole at the approximate focal distance from the lens that was screwed into the polarizing beamsplitter cube and linearly translated it until it was at the position where the beam spot had the smallest diameter (i.e., at the focal point) and mounted it in place. Initially I did this manually but then realized for this to be more repeatable, the z-position should be adjusted using a linear translation stage. Once the pinhole was in place at the focal plane indicated by the focused red dot in c of Figure 3-15, I removed this alignment laser, shown on the bottom left of part a. Part b shows the beam at an out-of-focus point, indicated by the larger spot size. Thus, the spatial filter was used to properly aligned the illumination source driven at a current of 8.8 mA. This is the total light that enters the remainder of the system for subsequent scans.

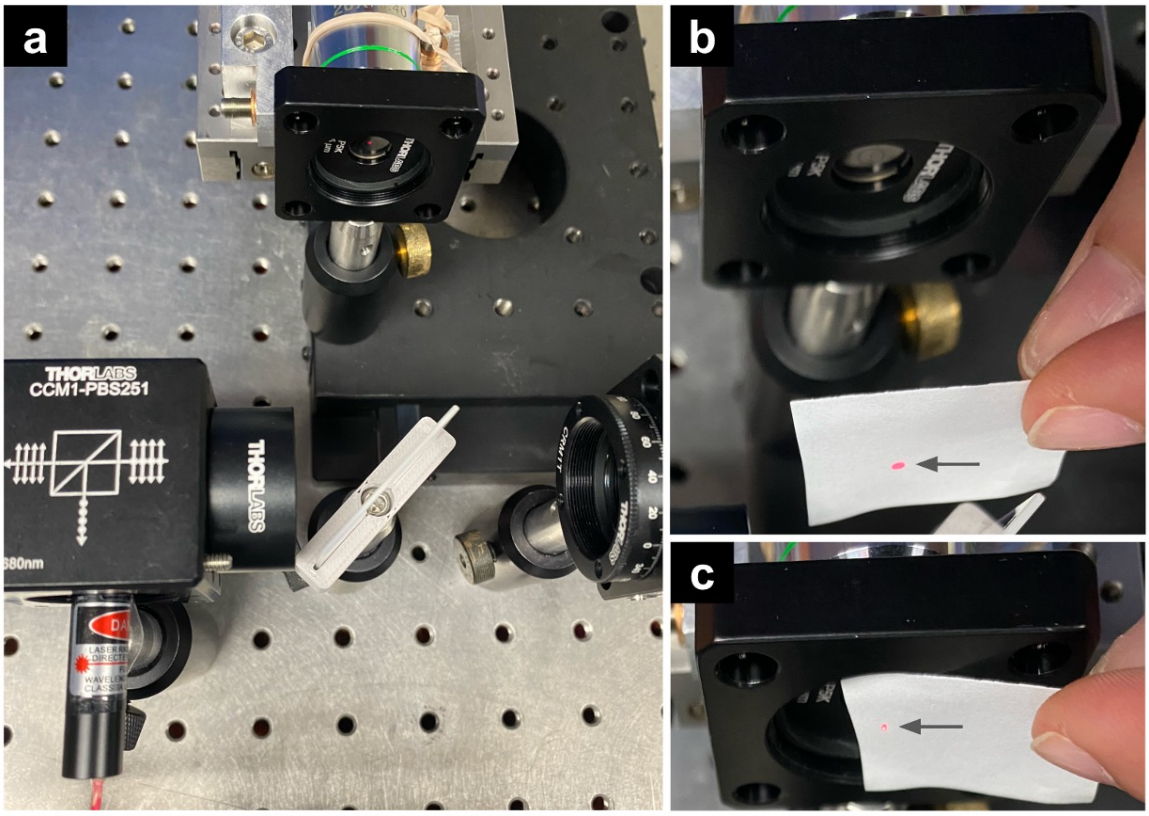

Figure 3-15: Laser alignment for pinhole positioning. (a) Laser alignment setup with proper alignment on the pinhole. Sweeping through the beam path through (b) unfocused regions to locate (c) the focal point.

The focal distance for high NA (i.e., high zoom) lenses is extremely small, and the design of 0.5" pinhole mounts and retaining rings makes it so that some objective lenses are physically blocked from getting close enough to reach the focus. Therefore, I opted to use a 1" mounted pinhole and flip the pinhole around such that it was closer to the objective lens.

3.2.4 Remaining Optical Elements

The light diverges from the pinhole towards the epi-illumination plate beamsplitter. The light that reflects off of the plate beamsplitter continues to diverge until it hits the lens, located one focal distance away from the pinhole. The lens collimates the light before it enters the polarizing beamsplitter cube, where it is separated into two orthogonally polarized paths. The transmitted beam continues along the straight path toward the reference mirror, while the reflected beam is folded by 90° through the polarizing beamsplitter cube toward the mounted sample. The blank cage plate mounted at the end of each of the two sides makes the structure rigid and prevents bowing and misalignment that could result from an unsupported lever arm.

3.3 Return Path

3.3.1 Overview

The light then reflects off of the reference mirror and sample surface towards the polarizing beamsplitter cube. When the beams reach the polarizing beamsplitter cube, the reference beam is transmitted through and the measurement beam is reflected, maintaining their respective polarizations. Following this, they pass through the collimating lens followed by a linear polarizer which has been rotated to equalize the transmitted power from the sample and reference arms. Additionally, the linear polarizer aligns the electric field vectors of the orthogonal sample and reference signals, allowing them to recombine and produce interference.

The behavior of the linear polarizer is described by Malus' law. For incoming light with equal orthogonal polarization components, $I_{\text{ref}} = I_{\text{sample}} = I_0$, and a linear polarizer oriented at $\theta = 45^\circ$ relative to the reference polarization axis, the transmitted intensity is

$$\begin{aligned} I_{\text{out}} &= I_{\text{ref}} \cos^2\theta + I_{\text{sample}} \cos^2(\theta - 90^\circ) \\ &= I_0 \cos^2 45^\circ + I_0 \cos^2(-45^\circ) \\ &= I_0 \left(\frac{1}{2}\right) + I_0 \left(\frac{1}{2}\right) \\ &= I_0 \end{aligned} \tag{3.11}$$

showing that the total transmitted power is exactly half of the total input, $I_{\text{ref}} + I_{\text{sample}} = 2I_0$, with an overall power loss of 50%. This is the case for a highly reflective flat sample such as a mirror, where virtually all of the light incident on the sample is returned straight back into the optical system.

In the more common case where most of the light incident on the sample is either absorbed or scattered away from the optical system, the relevent condition is $I_{\text{sample}} \ll I_{\text{ref}}$. To maintain good fringe contrast, the linear polarizer must be rotated to an angle that equalizes these beam powers. That means transmitting nearly all of I_{sample} while blocking most of I_{ref}. As a result, the total power passed through the linear polarizer approaches $2I_{\text{sample}}$ for such low reflectivity samples.

After passing through the linear polarizer, the recombined beam then enters the camera, which was pre-focused at infinity before being added to the system and placed at the focal point of the achromatic doublet, ensuring that the sensor captures a sharply focused interference pattern across the field of view.

The optical power returning from the measurement surface and ultimately reaching the camera (BFS-U3-13Y3C-C USB 3.1 Blackfly® S, Color Camera) is determined by the incident power together with attenuation at the sample. In particular, it depends on the sample absorbance, scattering behavior, and on a depolarization coefficient associated with surface roughness, which can range from 0.5 to 1. Rougher, less reflective surfaces can

therefore introduce additional effective attenuation by reducing the fraction of reflected light that remains in the desired polarization state.

3.3.2 Field of View

This system achieved a complete field of view of 1.4 cm by 1.1 cm, constrained only by the size of the image sensor. Given that it contained a 1280 by 1024 array of pixels, the digital resolution was calculated to be

$$r_{\text{dig},x} = \frac{\text{horizontal dimension}}{\text{horizontal pixel count}} = \frac{1.4 \text{ cm}}{1280} = \frac{14{,}000\ \mu\text{m}}{1280} = 10.9\ \mu\text{m/pixel} \tag{3.12}$$

$$r_{\text{dig},y} = \frac{\text{vertical dimension}}{\text{vertical pixel count}} = \frac{1.1 \text{ cm}}{1024} = \frac{11{,}000\ \mu\text{m}}{1024} = 10.7\ \mu\text{m/pixel} \tag{3.13}$$

The slight discrepancy between the horizontal and vertical digital resolutions arises from uncertainty in the measured image dimensions, which were approximated as 1.4×1.1 cm^2.

3.3.3 Lateral Resolution

The effective numerical aperture of an optical system is limited by the most restrictive element in the optical path which may be lower than the nominal NA of the objective if the pupil is underfilled or the beam is otherwise aperture-limited. In this case, the numerical aperture (NA) of the imaging lens determines the minimum achievable spot size and therefore sets a physics-based limit on lateral resolution. For a lens of diameter D, focal length f, and immersion medium (i.e., air) refractive index n, the numerical aperture can be written as

$$\text{NA} = n \frac{D/2}{\sqrt{f^2 + (D/2)^2}}. \tag{3.14}$$

For the present system, the achromatic doublet used has a focal length $f = 80$ mm and diameter $D = 25.4$ mm. Substituting these values gives

$$\text{NA} = 1 \cdot \frac{25.4/2}{\sqrt{80^2 + (25.4/2)^2}} = 0.157. \tag{3.15}$$

The corresponding diffraction-limited lateral resolution may be estimated using Equation (2.10). Using the design wavelength of 650 nm for the system and the NA of 0.157 gives

$$r_{\text{spot}} = \frac{0.650\ \mu\text{m}}{2(0.157)} = 2.07\ \mu\text{m}. \tag{3.16}$$

which corresponds to a spot size of approximately 2.1 μm. This means that the system's lateral resolution is limited by the size and resolution of the camera's image sensor rather than the underlying physics. Consequently, using a higher resolution camera can trivially improve the lateral resolution by ∼5x from ∼ 10.8 μm to 2.1 μm without any additional changes.

3.4 Select Future Modifications

In the future I intend to eliminate the plate beamsplitter and instead use the polarizing beamsplitter cube for epi-illumination, which should substantially increase the photon efficiency of the system. This could be accompanied by replacing the single lens that precedes the polarizing beamsplitter cube in the present design with two higher NA lenses that come after it, one for each arm. Since higher NA lenses have smaller focal distances, this would ensure that the focus would not reside within the polarizing beamsplitter cube. Higher NA lenses would make the system suitable for measuring less reflective samples, but would not be able to accommodate as large of a field of view and travel range as lower NA lenses.

I also plan to add a polarizer just after the pinhole to be able to select how much light is sent to the sample versus the reference. The goal is to balance the illumination of the interfering

beams as seen by the camera after passing through the second polarizer set to equally pick from the reference and sample beams with an angle of 45°, thereby maximizing the fringe contrast, where fringe contrast (or fringe visibility) is a measure of interference quality defined as the normalized ratio between the maximum and minimum beam intensities (or bright and dark fringes) in an interference pattern.

This setup used a Blackfly camera that was available in the lab since it was suitable for initial prototyping but was not selected due to holistic performance advantages over other cameras. In the future, a more specialized camera should be chosen to better match the demands of white-light interferometry, where accurate fringe measurement is critical. Key considerations include sensor resolution, where smaller pixel sizes improve lateral resolution of surface features, and field of view, where a larger sensor array enables imaging of a wider area. The camera should also support sufficiently high frame rates to accommodate scanning without excessive acquisition time. Similarly, a monochrome camera is superior because a color camera is effectively discarding 2/3 of the pixels associated with the unused colors. Beyond this, high bit depth and dynamic range are essential for resolving subtle intensity differences in interference fringes, directly impacting measurement accuracy.

Chapter 4

Mechanical Design

I designed a precision motion system to mechanically scan samples through the coherence plane using a combination of off-the-shelf, 3D-printed, and CNC-machined components. Since the sample should be in focus when it passes through the coherence plane, moving the sample is strongly prefered to moving the reference mirror. The system consists of a 3D-printed linear flexure driven by a precision hex screw, which is turned by a compact NEMA 8 motor with a 19:1 reduction. The motor is mounted to the carriage of a preloaded recirculating ball-bearing linear rail using a custom 3D-printed PETG bracket, enabling smooth, low-friction motion. As the motor steps, the coupled hex screw advances through a bushing embedded in the aluminum mount, pushing the flexure and attached sample in a precise and controllable manner. The flexure also provides preloading for the motion system, and because the mechanism operates in a single direction, backlash is eliminated.

4.1 Motor

I used a NEMA 8 stepper motor with a 19:1 planetary gearbox to drive the sample motion. Stepper motors provide repeatable, digitally controlled positioning with simple hardware. Since the scan was always in one direction and the system was preloaded with a spring, backlash effects were negligible. The NEMA 8 was chosen because it is compact, lightweight

(130 g), and met the precision requirements of the system without needing microstepping, which can sometimes introduce nonlinear behavior.

The NEMA 8 motor was attached to the MGN9H carriage of a 100-mm pre-loaded recirculating ball-bearing MGN9 linear rail made of bearing steel using a custom 3D-printed PETG bracket. This enabled smooth, low-friction motion of the motor assembly along the travel direction as the precision hex adjuster was screwed into the bushing.

4.1.1 Scan Rate

The Nyquist limit dictates that the sampling rate must be greater than twice the highest frequency component of interest in the measured signal in order to capture sufficient information to reconstruct it. The Nyquist limit can be defined in terms of wavelengths to apply to a spatial system such as that of the optical profilometer as shown below.

$$\tau_s = \frac{\lambda}{2} \tag{4.1}$$

where τ_s is the Nyquist limit and λ is the wavelength of the light source.

Since the optical path in the optical profilometer is folded, the standard definition of the Nyquist limit should be divided by an additional factor of two.

$$\tau_s = \frac{\lambda}{4} \tag{4.2}$$

Here, the scan rate was set to 50% of the Nyquist limit to capture all necessary information without unnecessarily slowing the scan.

$$v_{\text{scan}} = \frac{1}{2}\tau_s FPS = \frac{\lambda}{8} FPS \tag{4.3}$$

where v_{scan} is the scan speed selected for use in the optical profilometer system and FPS is the camera frame rate. Plugging in the wavelength in microns and frames per second, this

becomes:

$$\boxed{v_{\text{scan}} = \frac{0.650}{8} * 40 = 3.25um/s} \tag{4.4}$$

Therefore, the motion system must be precise enough to achieve this slow scan rate. Considering the gear ratio of the motor and the use of a fine hex adjuster with 100 threads per inch, the linear distance traveled per revolution of the motor shaft (before the gearbox) is:

$$umPerRev = \frac{p}{i} = \frac{254}{19} \approx 13.4um \tag{4.5}$$

where p is the precision hex screw's thread pitch in microns and i is the gear ratio.

4.1.2 Torque Analysis for Flexure Actuation

The pull-out torque curve in the motor's datasheet indicates the maximum torque the motor can produce without losing steps at a given speed. At 14.6 rpm, this motor can deliver up to $0.3\,\text{N}\cdot\text{m}$ of torque at the RMS rated current of 0.4 A, which must be sufficient to drive the screw against both friction and the flexure load. For the system in this thesis, a current of 0.2 A was selected to reduce heat dissipation and subsequent thermal expansion effects. Since stepper motor torque is approximately proportional to the applied current at low speeds, the maximum torque available at this lower current of $I_{\text{set}} = 0.2$ A can be estimated by linear scaling:

$$\tau_{\text{max}} = \tau_{\text{graph}} \times \frac{I_{\text{set}}}{I_{\text{RMS}}} = 0.3 \times \frac{0.2}{0.4} = 0.15\ \text{N}\cdot\text{m}.$$

At this low output speed, dynamic torque losses are negligible, so this represents the maximum torque the motor can deliver. Based on this, 0.15 Nm must be sufficient to drive the screw against both friction and the flexure load for this motor to work in the system. Since the flexure behaves approximately like a linear spring, its force response can be described using Hooke's law.

To estimate the torque required from the motor, I related the axial force-displacement behavior of the mechanism to the linear travel of the lead screw. The screw advances by one thread per full revolution. For a screw advance of 0.01 in/rev, the linear displacement

per revolution is

$$\Delta x_{\text{rev}} = \left(\frac{1}{100}\right)(0.0254) = 2.54 \times 10^{-4} \text{ m/rev.} \tag{4.6}$$

Since one full revolution corresponds to 2π radians, the linear advance per radian is

$$\Delta x_{\text{rad}} = \frac{\Delta x_{\text{rev}}}{2\pi} = \frac{2.54 \times 10^{-4}}{2\pi} \approx 4.04 \times 10^{-5} \text{ m/rad.} \tag{4.7}$$

The axial force was modeled as a linear function of displacement based on the measured flexure response under load. A linear fit to the experimental data gave

$$F(x) = kx + b, \tag{4.8}$$

where $k = 2000$ N/m is the fitted slope and $b = -1.0264$ N is an offset term associated with fitting error. Because this intercept is non-physical, only the linear term was retained in the torque calculation, giving Hook's law,

$$F(x) \approx kx. \tag{4.9}$$

A more detailed description of the flexure load experiment and brief FEA analysis is provided in the following section.

The starting displacement for this calculation was taken to be

$$x_0 = 0.02 \text{ m.} \tag{4.10}$$

The work required to move the screw forward by a linear distance Δx from the starting position x_0 was computed by integrating the axial force over displacement:

$$E(\Delta x) = \int_{x_0}^{x_0+\Delta x} F(x)\,dx. \tag{4.11}$$

For one full revolution of the screw, $\Delta x = \Delta x_{\text{rev}}$ and $\Delta x_{\text{rev}} \ll x_0$, so this integral simplifies to

$$E(\Delta x_{\text{rev}}) \approx k x_0 \Delta x_{\text{rev}}. \tag{4.12}$$

Evaluating this expression with the experimentally-determined spring constant $k = 2000$ N/m, $x_0 = 0.02$ m, and $\Delta x_{\text{rev}} = 2.54 \times 10^{-4}$ m gives

$$E(\Delta x_{\text{rev}}) = (2000)(0.02)(2.54 \times 10^{-4}) \approx 0.01 \text{ J}. \tag{4.13}$$

Using rotational work, linear and angular work are related by

$$F\,\Delta x = \tau\,\Delta\theta, \tag{4.14}$$

so the average torque over a displacement interval can be written as

$$\tau_{\text{avg}} = \frac{E(\Delta x)}{\Delta\theta}. \tag{4.15}$$

The angular displacement associated with a linear travel of Δx is

$$\Delta\theta = \frac{\Delta x}{\Delta x_{\text{rad}}}, \tag{4.16}$$

so for one full revolution,

$$\tau_{\text{avg}} = \frac{E(\Delta x_{\text{rev}})}{2\pi}. \tag{4.17}$$

Substituting the computed energy gives

$$\tau_{\text{avg}} = \frac{0.01 \text{ N m}}{2\pi} = 0.0016 \text{ N m}. \tag{4.18}$$

I also computed the instantaneous torque at the starting displacement x_0 by multiplying the axial force at that position by the screw advance per radian as a way to validate the previous calculations:

$$\tau_{\text{inst}}(x_0) = F(x_0)\,\Delta x_{\text{rad}}. \tag{4.19}$$

Evaluating this expression at $x_0 = 0.02$ m gives

$$\tau_{\text{inst}}(x_0) = F(x_0)\,\Delta x_{\text{rad}} = (2000 \cdot 0.02)\left(4.04 \times 10^{-5}\right) = 0.0016 \text{ N m}. \tag{4.20}$$

The average and instantaneous torque values are very close, differing only slightly because the axial force increases slightly over the small displacement corresponding to one screw revolution. Based on both calculations, the required motor torque is approximately

$$\tau \approx 1.6 \times 10^{-3} \text{ N m}. \tag{4.21}$$

Comparing this to the maximum torque output of the motor, $\tau_{\text{max}} = 0.15\,\text{N} \cdot \text{m}$, it is clear that the selected motor handily meets the system requirements for driving the flexure through the 2-cm travel, being capable of nearly 100 times the required torque while minimizing size.

4.2 Interfaces

4.2.1 Shaft Coupler

The gearbox was attached to the precision hex adjuster using a custom 3D-printed shaft coupler. This flexible shaft coupling type was chosen to dampen vibrations and account for any minor shaft misalignment, and set screws were used to securely attach the coupler to the gearbox shaft and precision hex adjuster, respectively.

Previously, I had designed and built a ruling engine that required shaft couplers, and I was frustrated at how expensive they were and vowed to make my own next time they were called for[24]. Here, I designed a clamping hub for the precision hex adjuster and another for the gearbox shaft and printed them out of PETG with 30% infill using a Prusa MK4S 3D printer. I also designed and printed a spider to go between them out of high-speed TPU. Adding double sided tape to either side of the spider was enough to keep them attached during scans. This reduced the shaft coupling materials' cost from approximately $65 to $0.11 ($0.06 for the spider and $0.05 for both clamping hubs combined according to PrusaSlicer). These are depicted in several figures, including Figure 4-1 and Figure 4-4.

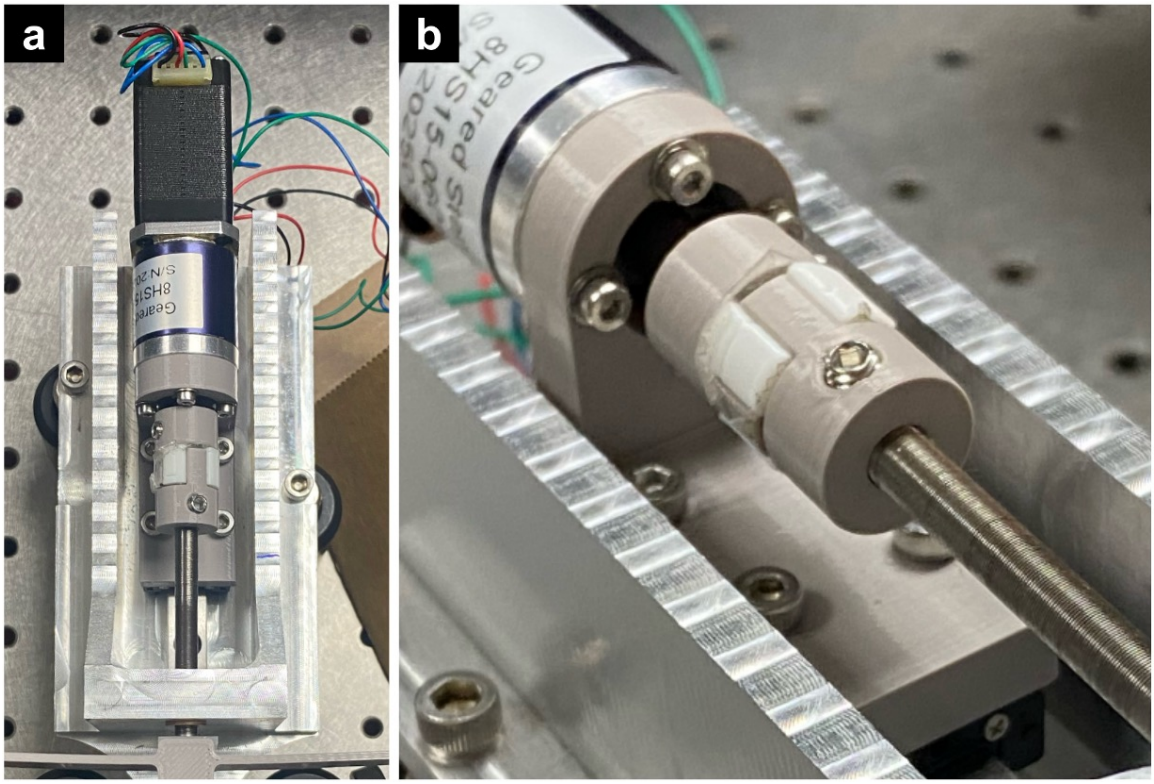

Figure 4-1: Shaft coupler. (a) Top-down view of the shaft coupler assembly and (b) zoomed-in view of the shaft coupler.

4.2.2 Bushing Holder

The precision hex adjuster functions as a lead screw, advancing through a threaded bushing to produce controlled linear motion. Initially I had designed the bushing mount to be 3D-printed out of PETG like the clamping hubs, but in practice, this allowed the bushing mount to deform with each revolution of the gearbox shaft, even when reinforced, causing substantial out-of-plane bobbing of the precision hex adjuster and the flexure it pushed.

In response to this observation, I redesigned the bushing holder to be CNC milled out of aluminum, which would be substantially stiffer and offer the rigid stability required to remove the cyclic hex adjuster wobble. This aluminum part also became the rigid structure that supported the entire motor assembly mounted on the linear rail.

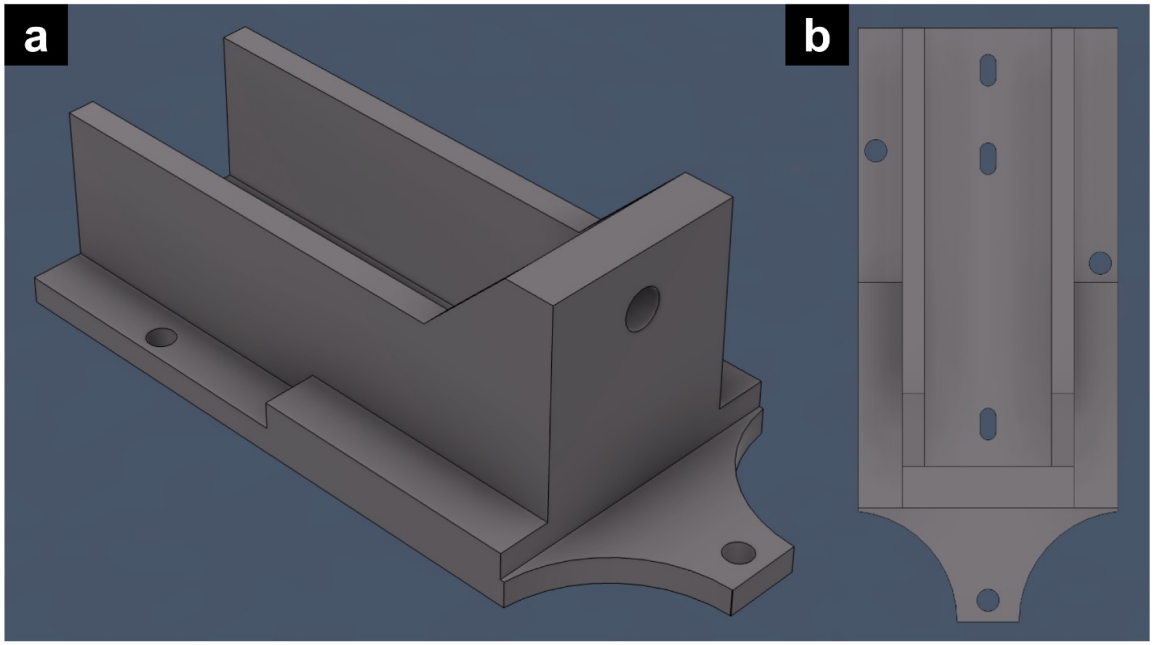

Figure 4-2: Bushing holder CAD. (a) Orthographic view of bushing holder design and (b) top-down view revealing hole positions.

After creating the CAM in Fusion 360, running the machine simulation, and addressing some post-processor bugs, I set up the aluminum stock in the Hurco VMX42SRTi 5 Axis Machining Center with some help from Dan Gilbert and Colin Marcus. I then machined the part, adjusting speeds and feeds as needed throughout the process in response to any rubbing or chatter. Here are some images detailing the machining process. This part required two mounting setups, so I designed the tall walls to make workholding easier once the part was flipped upside down in preparation for the second round of machining. Note that it is important to re-probe the workpiece for the second set of operations using the same corner as the one that was probed before the first set of operations to minimize misalignment artifacts. The bushing hole was machined using a 1/4" end mill in a 3+2 indexed machining operation, where the rotary axes positioned the part and the hole was milled using the three linear axes.

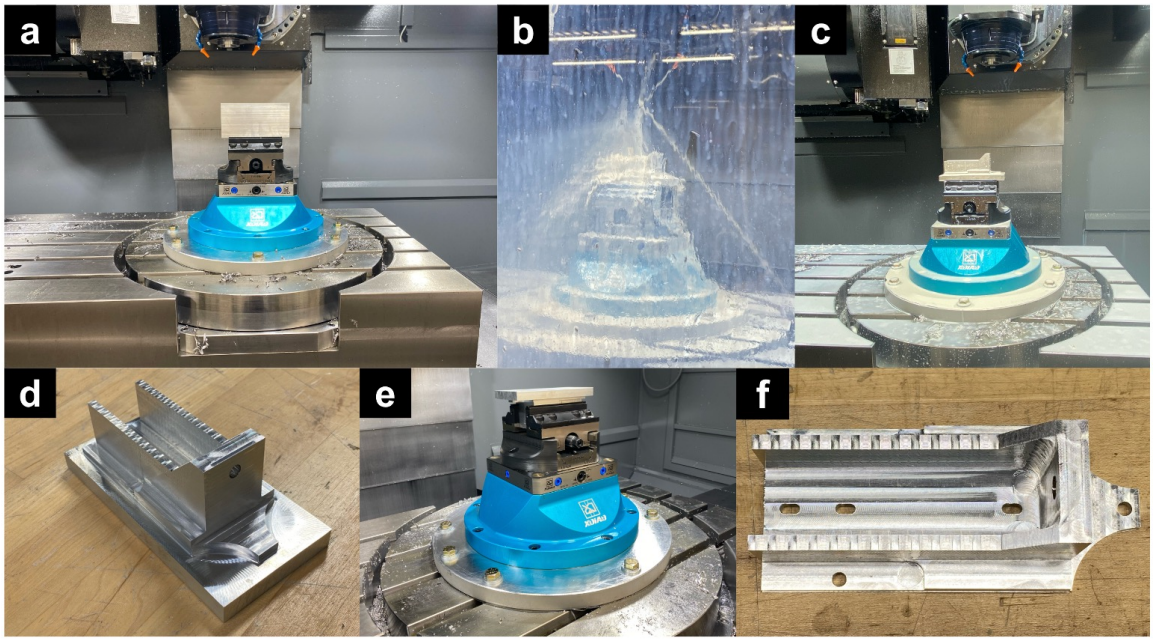

Figure 4-3: Machining bushing holder on 5-axis milling machine showing (a) initial setup, (b) machining with coolant, (c) resulting part in workholding, (d) removed part with tall walls to make workholding easier, (e) second setup, and (f) completed part with drill holes from second setup.

To prevent the bushing threads from becoming contaminated, the ends of the bushing were taped shut prior to sanding its sides to create a rough texture that would better adhere to the inside of the aluminum bushing holder with a thin layer of adhesive. To apply the adhesive, I added a drop of Gorilla Super Glue XL to a paper towel, scooped a very minimal amount up using a toothpick, and coated the inside of the bushing mount with it, removing any excess to prevent glue from contaminating the screw threads. Then I added the bushing in a single pushing motion, keeping in mind that the Gorilla Super Glue XL begins to cure in about 10 seconds so there can be no repositioning. If there is too much glue and the threads become contaminated, it can be chemically softened with IPA, and a precision hex adjuster can be manually threaded through to clear the debris. However, it is best to avoid adding excessive adhesive and needing this fix since the bushings are pre-lubricated for enhanced smoothness, and IPA strips bushings of this lubrication. The following images were taken prior to replacing the flexure adapter plate with the new version.

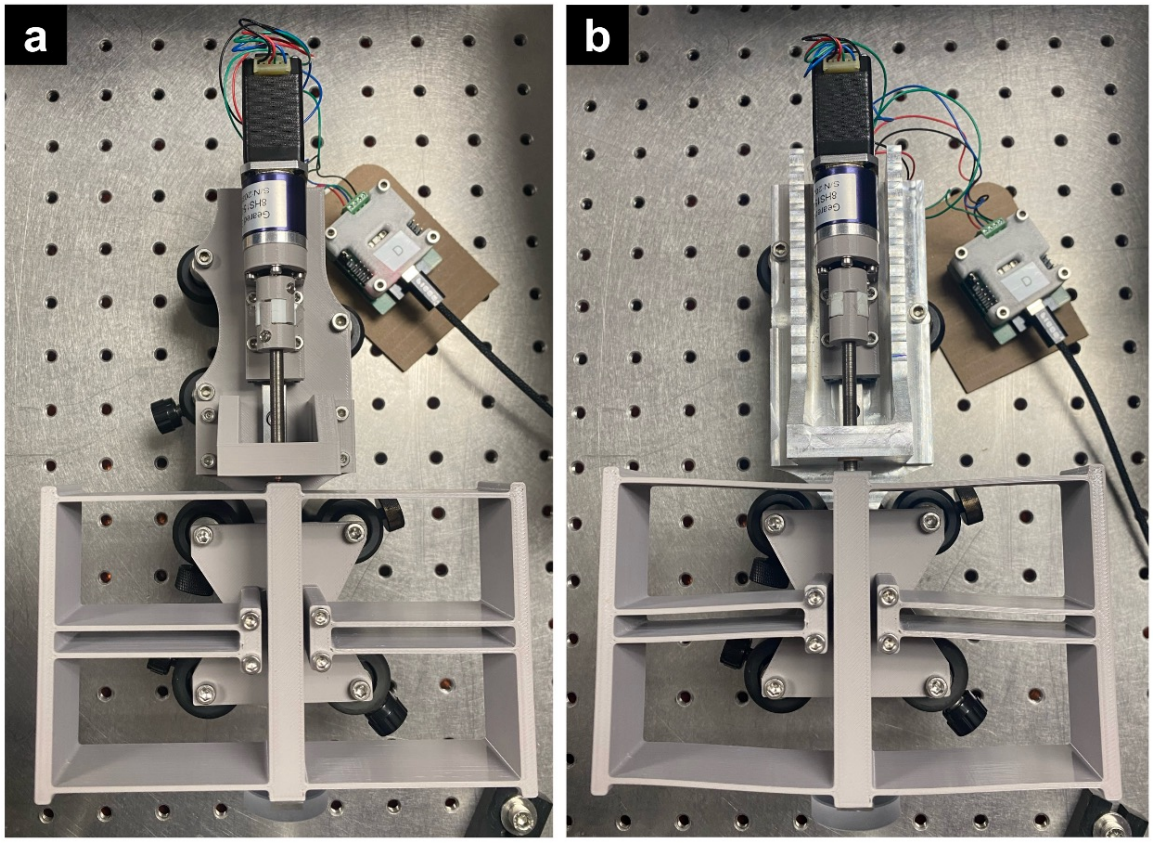

Figure 4-4: Machined bushing holder replacement for PETG design. (a) 3D-printed PETG precursor to the (b) aluminum bushing holder design, integrated into the mechanical system.

4.2.3 Flexure Surface

The precision hex adjuster was selected to have a ball tip to ideally provide a single point of contact with the flexure surface. However, since the flexure is 3D printed, the uneven surface resulting from layer lines causes the precision hex adjuster to "walk" across the surface. This transfers non-axial forces to the flexure, causing it to bob.

To avoid this, a glass slide was cut to size and adhered to the flexure surface to serve as a smooth contact surface between the flexure and the precision hex adjuster. With this modification, the contact was substantially improved, and the precision hex adjuster no longer "walks" along the surface, largely constraining the transferred forces to the axial direction. This mechanically isolates the flexure motion from the linear translation of the

motor, as the only thing driving the flexure motion is the turning of the precision hex adjuster.

However, at higher forces, the tip of the precision hex adjuster begins to carve into the glass slide, which makes subsequent scans reveal noticeable bobbing over long time scales. Due to this realization, I discovered that I needed to use a harder material than glass for this purpose. Sapphire has exceptionally high hardness around 2,000 MPa[25] and is readily available in both microscope slide and optical window form. I replaced the glass slide with a 1/2" optical window to preserve the smooth contact while preventing carving of the surface. Because the sapphire is transparent, the adhesive between it and the flexure look like surface roughness even where none is actually present. The sapphire window was purchased for about $50 from Thorlabs[17], but much cheaper options are also available.

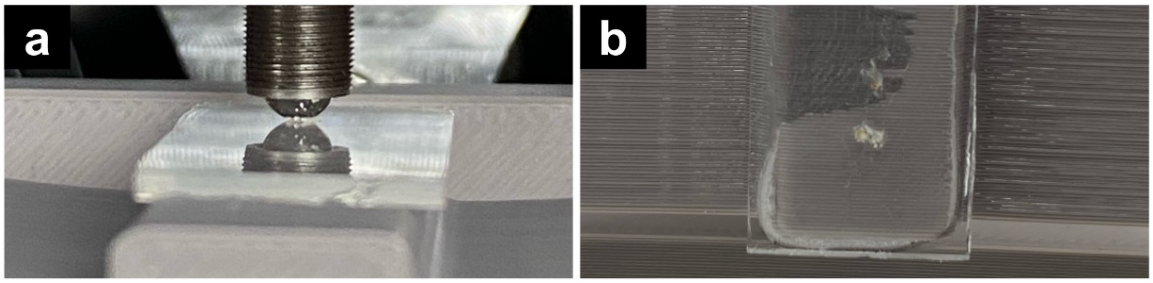

Figure 4-5: Glass interface.

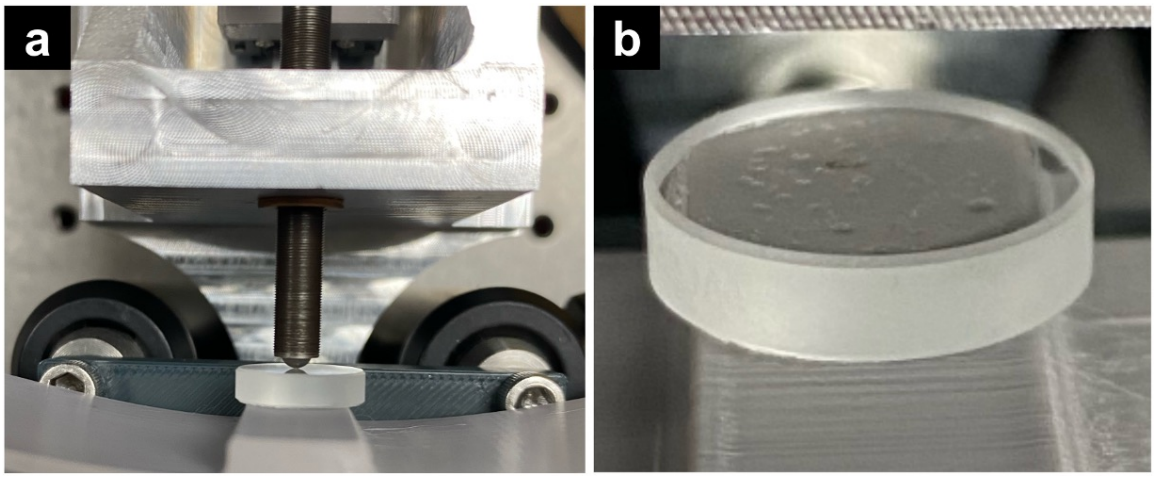

Figure 4-6: Sapphire interface.

Samples were initially mounted to the end of the flexure by double-sided gel mounting tape to the flexure surface, but regular double-sided tape was ultimately used to avoid any potential effects of gel tape creep. I initially included a supportive shelf feature to facilitate more repeatable positioning, but it was later removed to facilitate the mounting of larger samples.

4.3 Flexure

4.3.1 Linear Translation Stage

To translate the sample through the coherence plane, precise linear motion is required. Initially, a conventional off-the-shelf z-axis translation mount from Thorlabs (SM1ZA) was used. This post-mountable stage provides only 2 mm of travel, requiring near-perfect alignment with the coherence plane to enable scanning. Consequently, even under optimal conditions, the measurable sample thickness was limited to less than 2 mm. The stage was originally operated manually and later motorized to facilitate automated scanning. However, due to its limited travel range, sensitivity to alignment, operational complexity, and cost of $235.61 (excluding custom motorization add-ons), it was ultimately replaced with a custom 3D-printed flexure stage capable of over 2 cm of travel. In the custom design, the distance between the carriage and the end of the linear rail is approximately 23.5 mm when the precision hex adjuster just makes contact with the glass slide on the flexure surface. Treating approximately 3.5 mm as a mechanical buffer yields an effective travel range slightly exceeding 2 cm, making it much easier to load and successfully scan samples without requiring careful measurement or alignment.

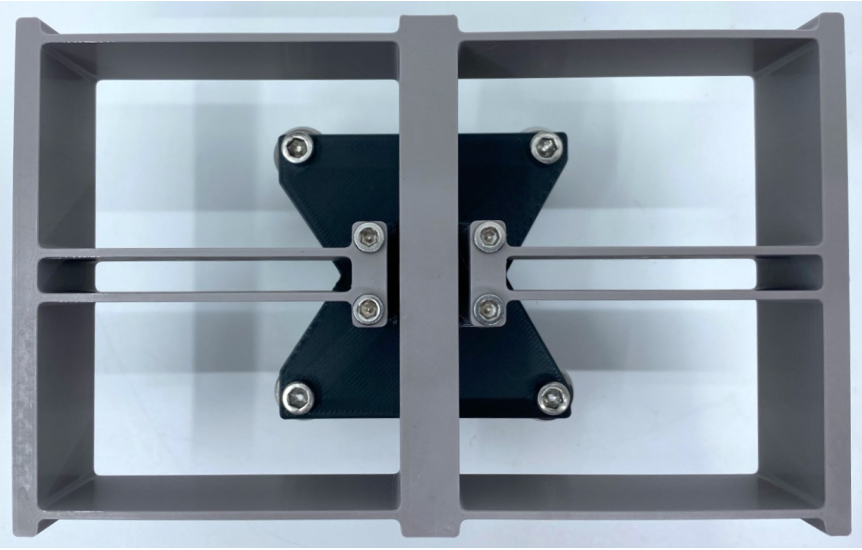

Figure 4-7: Flexure.

I designed the flexure to serve as a linear translation stage because flexures produce smooth, predictable motion through elastic deformation rather than sliding or rolling contact, eliminating friction. This is also why the flexure is suspended on an adapter plate rather than sliding on another surface. The compound double-parallelogram linear flexure design also allows motion in the desired linear direction while remaining stiff in other directions, helping maintain alignment and positional accuracy. Alignment is crucial to ensure motion occurs exclusively in the axial direction. Therefore, I have added alignment markers to the flexure adapter plate to constrain the mounting position such that the flexure's linear translation axis is orthogonal to the polarizing beamsplitter surface. Additionally, the flexure acts as a spring that preloads the precision hex adjuster, removing backlash. This is depicted in the mechanical testing section in Figure 4-9.

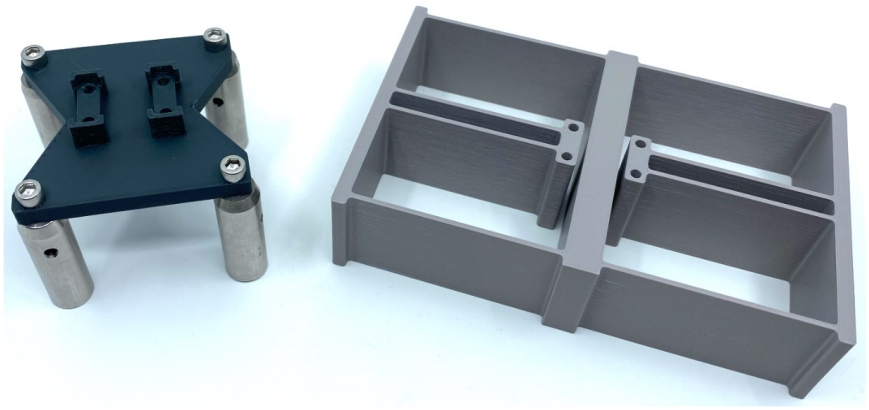

Figure 4-8: Flexure adapter plate.

4.3.2 Degrees of Freedom and Design Tradeoffs

The flexure stage is designed to enable precise linear translation of the sample through the coherence plane while constraining unwanted motion. In an ideal implementation, five of the six degrees of freedom would be constrained, allowing only translation along the axial scanning direction. These six degrees of freedom consist of linear translation along the x, y, and z axes, as well as rotation about each of these axes.

In the present design, the axial direction is defined as the z-axis. The flexure constrains motion in four degrees of freedom: translation along x and y, and rotation about the y- and z-axes. Here, the x-axis corresponds to the lateral width of the flexure, while the y-axis corresponds to the out-of-plane direction. These constraints are achieved by rigidly fixing the inner regions of the flexure using screws, which restrict lateral and out-of-plane motion as well as associated rotations. As a result, translation along z and rotation about the x-axis remain relatively unconstrained.

In an earlier iteration of the design, the unconstrained rotational degree of freedom led to noticeable out-of-plane motion ("bobbing") during operation of roughly 16 um. To mitigate this effect, the flexure thickness was increased along the z-direction, improving stiffness and reducing susceptibility to unintended rotation.

Despite this improvement, rotation about the x-axis remains insufficiently constrained. Fu-

ture design iterations will focus on directly limiting this degree of freedom while preserving the desired axial compliance. However, since the force applied by the precision hex adjuster are almost exclusively in the z-direction, only minimal off-axis effects are observed with the greater flexure thickness.

The design of the flexure stage involves several competing tradeoffs between travel range, stiffness, degree-of-freedom constraints, form factor, and ease of fabrication. Achieving a large travel range favors more compliant structures, which can undergo greater elastic deformation. However, increased compliance also makes the system more susceptible to off-axis motion and deformation in unconstrained directions. Conversely, increasing stiffness improves stability but reduces the achievable displacement.

Several design choices reflect these tradeoffs. The anchor points were positioned closer to the center of the flexure to increase stiffness and improve overall stability. Additionally, rotation about the y-axis is constrained by using two screws at each anchor point, separated along the z-direction. Increasing the spacing between these screws improves resistance to rotational motion; however, it also reduces the available travel range. Therefore, the screw spacing was minimized while using sufficiently large fasteners to maintain reliable fixturing.

Material selection also plays a critical role in these tradeoffs. More compliant materials enable larger displacements but at the cost of reduced directional stability. While stiffer materials improve resistance to off-axis deformation, they do not inherently change the ratio between linear displacement and parasitic motion. In principle, an anisotropic material with high stiffness in the y-direction and lower stiffness in the z-direction could provide improved directional stability while maintaining a large travel range, which would make an interesting extension to this work. For prototyping purposes I mounted everything on posts on an optical table and used an adapter plate for the flexure. This can be done away with in future iterations.

4.3.3 Mechanical Characterization

The flexure was mechanically characterized using an Instron 4411. A small tab was added to the flexure to allow the clamps to grip onto it. The flexure was mounted in much the same was as it is in the optical profilometer system, onto a bracket that could be mounted onto an optical table at the base of the Instron.

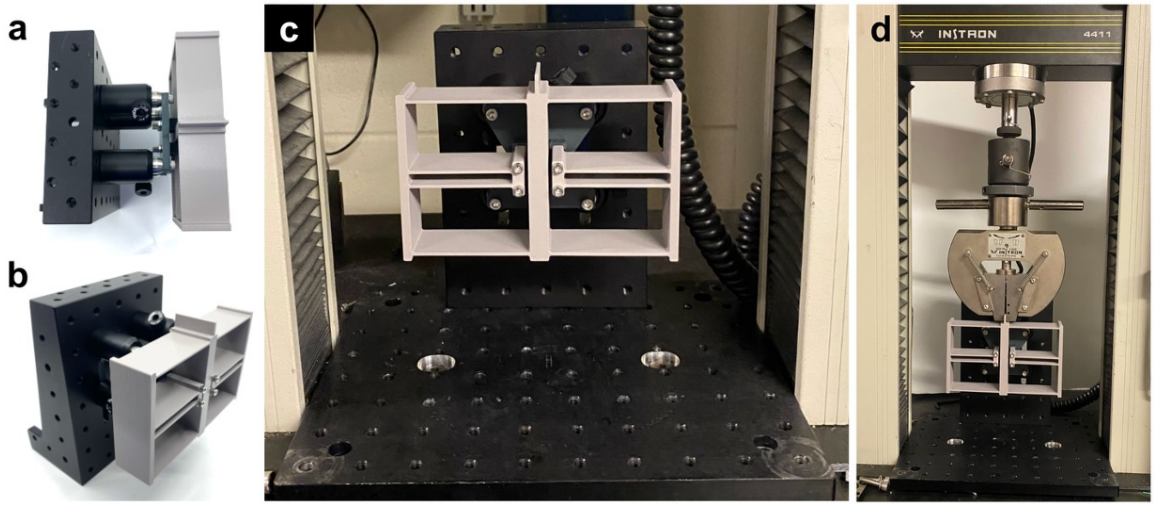

Figure 4-9: Flexure setup for mechanical testing. (a) Top view and (b) isometric view of mounted flexure. (c) Zoomed-in view of flexure mounted onto the optical table at the base of the Instron 4411 and (d) a zoomed-out view of the entire test setup with jaws clamped onto the flexure tab.

An extension test was performed using a 5 kN load cell at a rate of 10 mm/min for a displacement of 2 cm. This was followed by a cyclic test for 100 cycles under the same conditions.

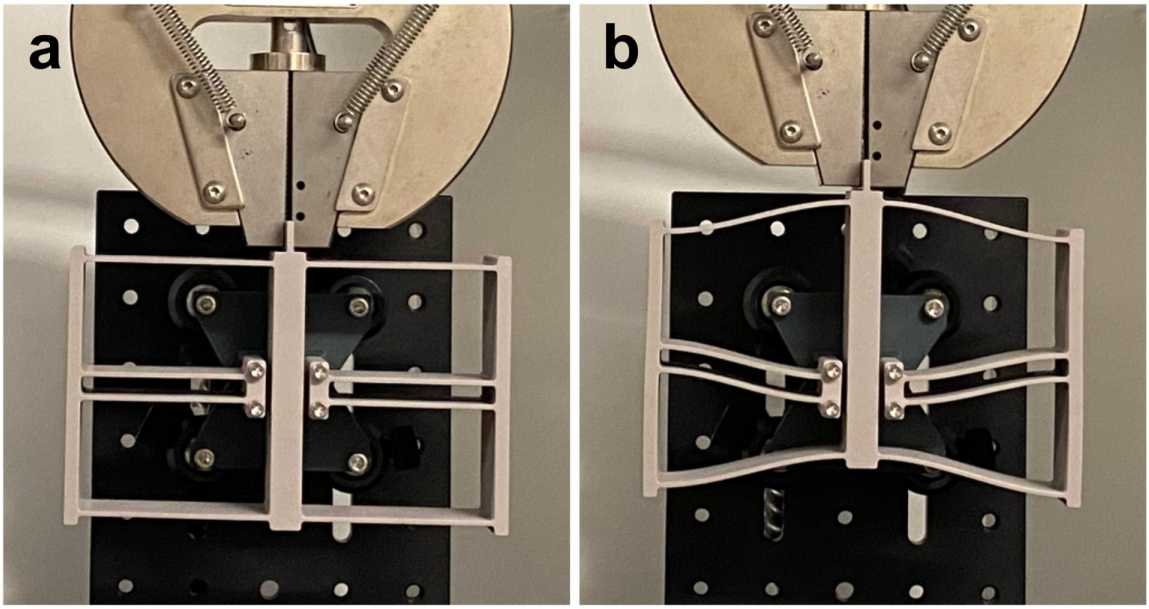

Figure 4-10: Mechanical testing of flexure at (a) no extension and (b) 2 cm extension.

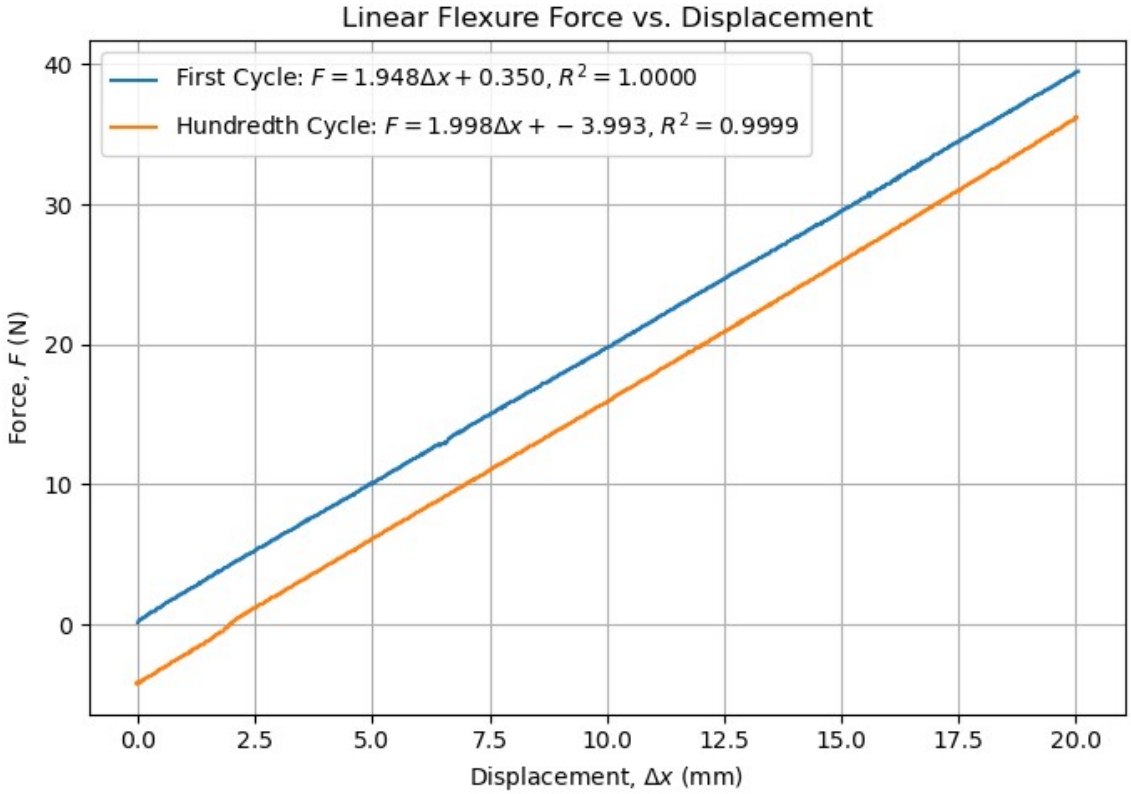

Figure 4-11: Flexure Instron data.

From this linear data, the spring constant of $\sim$ 2 N/mm (or $\sim$ 2000 N/m) could be extracted. There appears to have been some minor drift of the Instron during the course of the experiment which caused the data from the hundredth cycle to be translated below 0 N on the force axis, but the force-displacement relationship remained constant throughout.

4.3.4 FEA Simulation

To define a custom material for the Fusion FEA model, I treated the 30% infill PETG print as a homogenized isotropic material and calculated approximate properties for density, Young's modulus, shear modulus, Poisson's ratio, yield strength, and tensile strength. This turned out to be an unrealistic approximation, since extruded PETG is anisotropic in practice and depends on factors such as print orientation, interlayer bonding, infill pattern, and layer thickness. However, a few qualitative takeaways can be made from the resulting FEA simulation. In Figure 4-12, red indicates values below the safety threshold (i.e., at risk of plastic deformation or failure), green indicates values that meet the safety threshold, and blue indicates values that comfortably exceed the safety threshold.

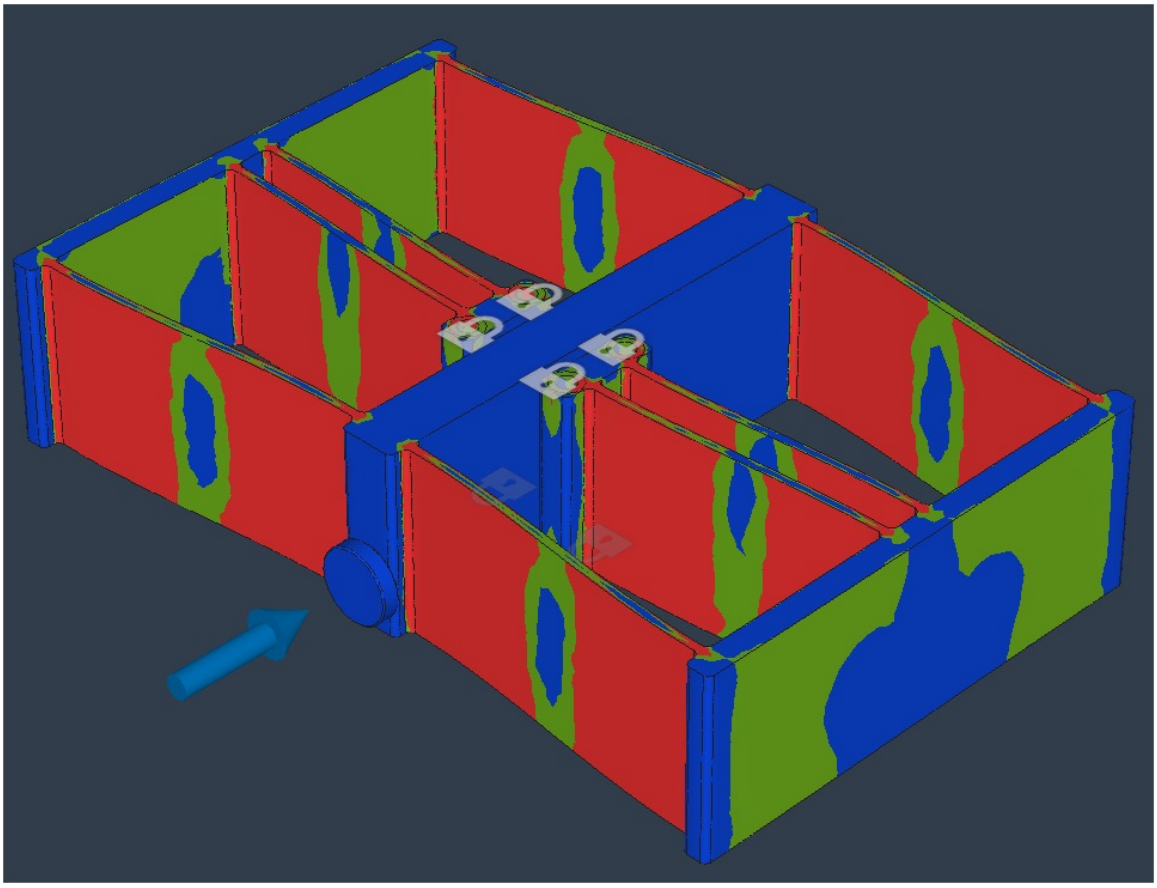

Figure 4-12: FEA results.

In Figure 4-13, a 40 N force was applied normal to the sapphire surface, and constraints were applied to the flexure where bolts and the 3D printed adapter plate constrain it in the optical profilometer setup. Firstly, the sapphire does not undergo mechanical deformation from the applied 40 N of force. Additionally, the deformation profile is similar to that observed experimentally, which is depicted below for a distance of 0, 0.5, 1.0, 1.5, and 2.0 cm. These images were taken before the glass slide was replaced with the sapphire window at the screw-flexure interface. This is also before the adapter plate was modified to include the position constraining slots.

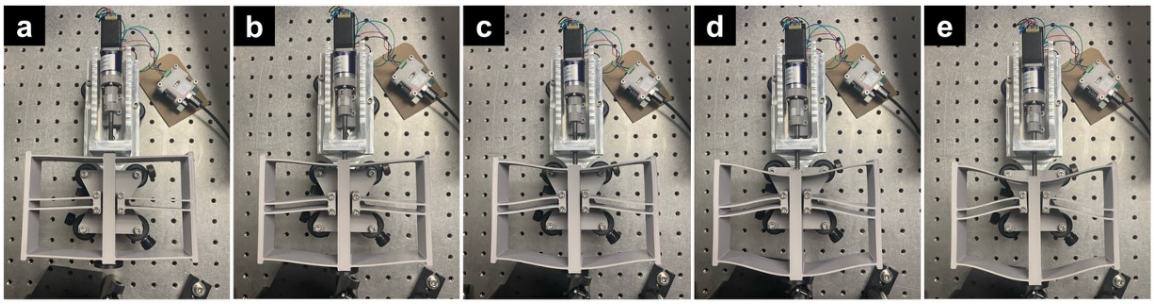

Figure 4-13: Flexure deformation across (a) 0, (b) 0.5, (c) 1.0, (d) 1.5, and (e) 2.0 cm.

Chapter 5

Computational Methods

5.1 Motor Control

To control the motor, I used Jake Read's modular motor controller boards and modified code from him and Quentin Bolsee to suit this application. The motor controller includes Jake's dual H-bridge board for stepper motors[26] which is a plug-and-play modular physical computing system presented as part of Modular-Things[27]. This allows the motor to be remotely controlled over USB connection.

5.2 Camera Capture

At this stage of development, camera capture is executed using the existing SpinView software for the Blackfly camera. The system was operated with a maximum ADC bit depth of 10, a bitrate of 2 Mb/s, and BayerRG16 encoding (16 bits per color channel per pixel). Gain was minimized whenever possible to minimize noise and images were captured at 40.00273 FPS. Remaining settings were adjusted as needed to enable the camera to register sufficient illumination from the sample without introducing excessive noise. In a future iteration, custom camera capture code can be developed to greatly reduce noise and processing time

since it can be designed to add frame count as metadata (which will circumvent the need for prescanning the entire video file during data processing), quantitatively determine optimal gain levels for parameter setting, and save images using lossless compression algorithms that can be reversed later to preserve information.

5.3 Signal Processing

5.3.1 Approach

The recorded video data was processed to identify the coherence signal at each pixel. As the sample was scanned in the axial direction, the intensity at each pixel varied with time. When the sample surface passed through the coherence plane, the pixel intensity exhibited a localized interferometric fluctuation (i.e., an intensity spike) because interference occurs only near where optical path-length matching between the reference and sample arms occurs. At positions away from the coherence plane, this interferometric modulation is weak or absent, and the remaining temporal variation is dominated primarily by slow drift, background offsets, and noise. The following filtering steps were therefore chosen to preserve the temporal variation associated with passage through the coherence plane while suppressing these other contributions. The characteristic duration of this coherence-related signal was estimated from the scan speed and the axial width of the coherence envelope, and this estimate was used to select the filter parameters. This is explained in more detail in the first test case below.

The first processing step was to high-pass filter the temporal intensity signal to remove slowly varying offsets, background illumination changes, and mechanical or thermal drift. In discrete form, filtering was implemented by convolution. For a temporal signal $x[n]$ and filter kernel $h[k]$, the filtered output $y[n]$ is given by

$$y[n] = \sum_{k} x[n-k]\, h[k].$$

Applying a high-pass filter in this manner suppressed components below the expected

coherence-plane flicker frequency, thereby enhancing the relative visibility of the localized interferometric response.

After high-pass filtering, the signal was squared to form a power-like quantity,

$$p[n] = y[n]^2.$$

This operation removed the sign of the oscillatory component and therefore eliminated phase reversals, leaving a strictly positive envelope that could be more robustly localized. In effect, this transformed the problem from detecting a rapidly oscillating interferometric signal to detecting the position of a localized burst in signal energy.

The resulting power signal was then low-pass filtered using convolution with a Gaussian kernel. This step acted as a smoothing operation motivated by matched filtering principles. In linear detection theory, the optimal filter for detecting a known signal shape in additive noise is one whose impulse response matches the expected form of that signal. Here, the coherence envelope is expected to be approximately Gaussian in time for an illumination source with a Gaussian-like spectrum, so a Gaussian kernel provides a practical approximation to a matched filter. For best performance, the kernel length should be chosen to be equal to the temporal width of the coherence signal, which is set by the coherence length and scan speed. Intuitively, the moving filter window should span the full duration of the expected coherence event so that the filtering operation integrates signal energy over the entire envelope rather than only a fraction of it.

Following this smoothing step, the square root of the filtered power signal was taken to return the result to the original signal units while preserving the envelope localization. The axial position corresponding to the maximum of this processed signal was then identified for each pixel. Repeating this procedure across all pixels yielded the recovered height map.

5.3.2 Implementation Details

Although the processing sequence described above is conceptually straightforward, practical implementation was challenging due to the size of the video dataset. A full scan consists of more than 10,000 frames, making it impractical to load the entire dataset into RAM and perform all convolutions directly on the complete time series at once. A memory-efficient implementation was therefore required.

To address this, the filtering operations were implemented using short convolution kernels and a streaming computation strategy. Rather than storing the entire dataset in active memory, only the subset of frames required for the current convolution step was loaded at any given time. This was accomplished using a ring buffer, which maintained a rolling window of the most recent frames relevant to the filter calculation. As new frames were loaded, the oldest frames were discarded, allowing the convolution to be evaluated incrementally with fixed memory usage.

This approach preserved the benefits of the convolution-based signal processing pipeline while making it feasible to process large datasets on available hardware. It also ensured that the matched-filter-style smoothing could be applied consistently across the full scan without requiring prohibitively large memory resources.

5.3.3 Noise

The camera has a noise floor that is primarily due to the Poisson statistics (i.e., shot noise) of incoming photons[28]. According to the PYTHON1300 datasheet[29] (the camera sensor in the Blackfly), the full well capacity is about 10,000 electrons, meaning that the best case scenario noise under bright illumination is $\sqrt{N} = 100$ or 1% of the signal, meaning the best case SNR ($20log_{10}(N/\sqrt{N})$) is 40 dB. This noise floor determines the measurement limit in dark regions of the image.

Initially, I used a coherent signal processing method on the data. For the coherent signal processing method, I started by using a band pass filter around the expected frequency,

which is based on both the linear translation speed and frame rate of the camera, followed by a Hilbert transform to make the signal complex valued and continuous. Finally I took the absolute value to get the envelope.

Axial positioning error due to flexure bobbing causes the phase to flip sign, so this approach runs into issues when this happens, which coincides with the phase error reaching π. This leads the pixel value to be incorrectly computed to be zero, resulting in harsh transitions between otherwise smooth gradients at pixels where the phase sign flipping occurs.

Because of this, I switched to an incoherent signal processing method to replace the coherent one. For the incoherent signal processing method, I first applied a high pass filter to eliminate the DC offset. Then I squared the pixels to remove the phase information, which circumvents the phase sign flipping issues that appear with the coherent signal processing method. Then I took a low pass filter to remove the noise floor and took a square root of the signal to get the envelope.

The drawbacks of this approach are that without the bandpass filter, the SNR of the signal is substantially degraded since the bandpass filter removes noise at all frequencies other than the coherence plane frequency. This means that the narrower the bandpass filter could be, the better the system would perform, especially for dark image regions. Switching to the incoherent highpass filtering method means that only the low frequency drift is removed without removing any of the remaining noise.

Additional noise sources include thermal noise from the camera, mechanical noise from the flexure wobble, and compression noise of the camera. More remains to be done to address these.

Chapter 6

Test Cases

6.1 Mirror

6.1.1 Axial Resolution Calculation

This chapter shows the results from a few scans I performed on different types of targets to get a better sense for how the system performs under different conditions at this stage of development. The first is a first-surface mirror. The gradient in the height map accurately shows the smooth, slightly angled mirror surface and also contains information about the overall optical profilometer system noise.

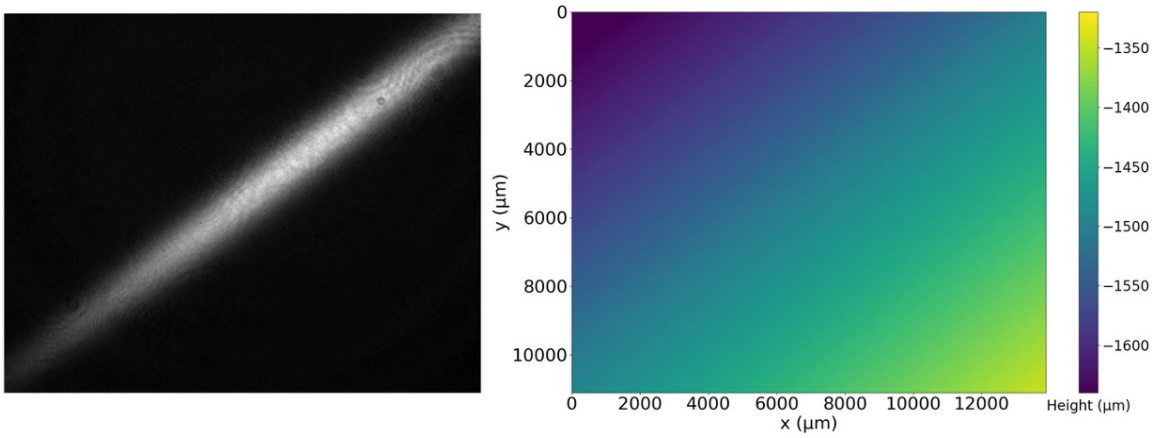

Figure 6-1: Mirror scan results. Coherence plane (left) and mirror height map (right).

The mirror is a good ground truth test case because the surface is known to be flat to $\lambda/10$[17]. The axial measurement error can be characterized by taking a row of pixels across the heightmap image and plotting it as a 1D waveform as shown in Figure 6-2. In the ideal case, this would look like a noise-free sloped line, and any deviation from that can be attributed to measurement error.

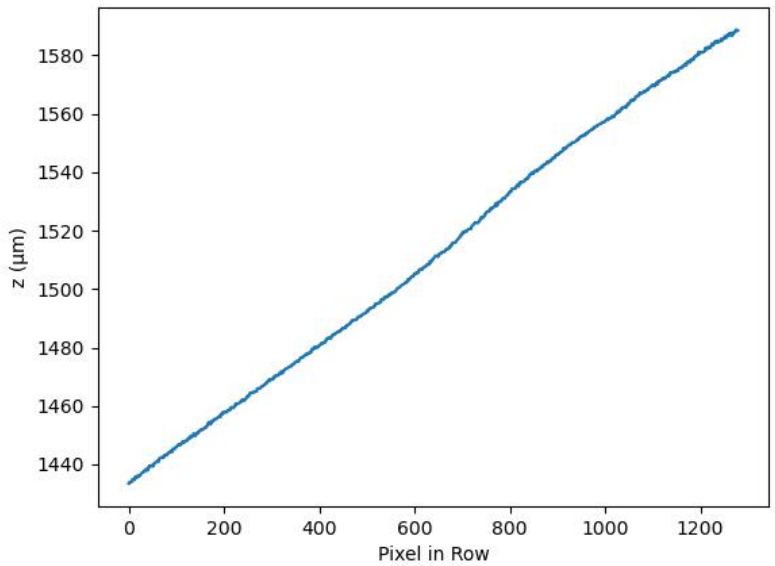

Figure 6-2: Linear plot of axial position versus row across mirror heightmap (1D waveform).

Detrending this waveform as in Figure 6-3 shows that the noise in the height map contains

both a low frequency component and a high frequency component. The low frequency can largely be attributed to remaining mechanical instability in the system primarily associated with the flexure's unconstrained degree of freedom about the x-axis. The magnitude of this low-frequency component is approximately 2 um.

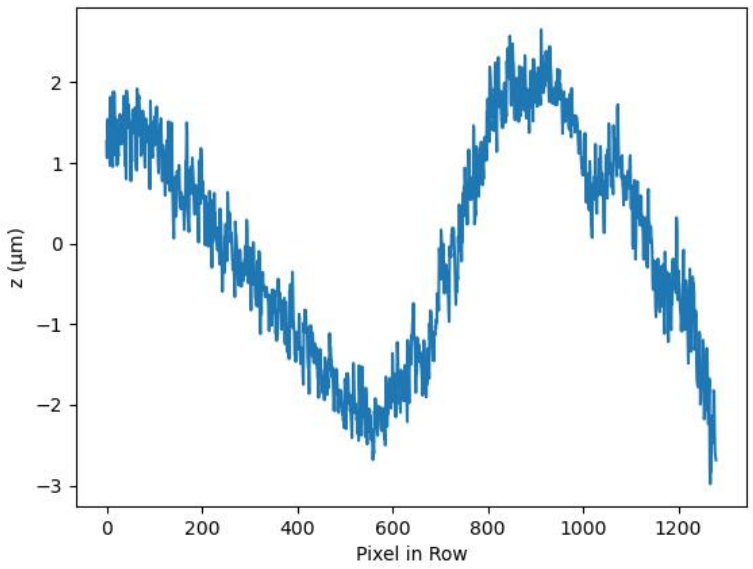

Figure 6-3: Low-frequency error in mirror scan.

In order to measure the RMS value of the high frequency measurement error, I high pass filtered the waveform (Figure 6-4) and then calculated the RMS value. Filtering out the low-frequency component to focus on the high-frequency component and taking the RMS of 100 rows of pixels results in an RMS value of 270 nm for the axial resolution.

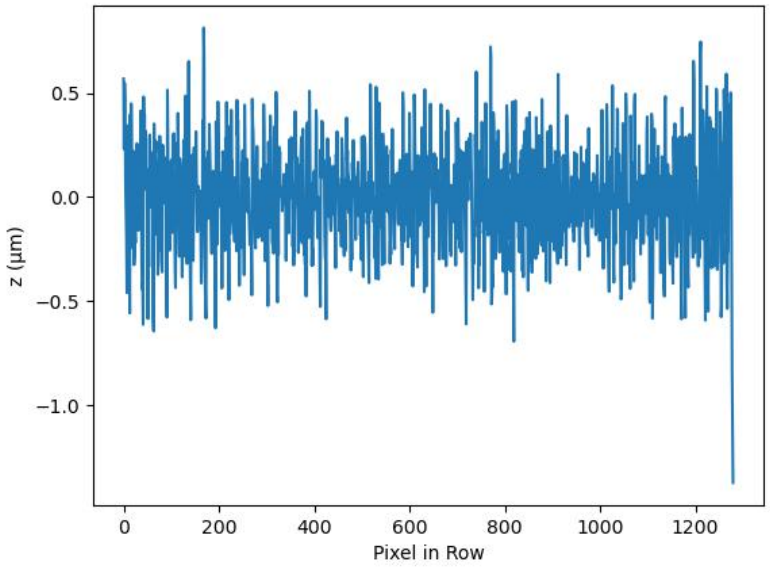

Figure 6-4: High-frequency noise in mirror scan.

6.1.2 Coherence Plane Calculation for Lateral Resolution

The coherence length (or coherence plane width) can also be calculated from this mirror scan. The procedure is as follows. First, take a single row of pixels from across a region of the mirror image that has a good signal. Then select a single pixel near the middle of the image that likewise has a good signal. Implement a similar processing algorithm to that used to recover the brightness peak. For recovering the coherence length, take a high-pass filter, then a Hilbert transform, and then take the absolute value to get the envelope. Then take a Gaussian fit.

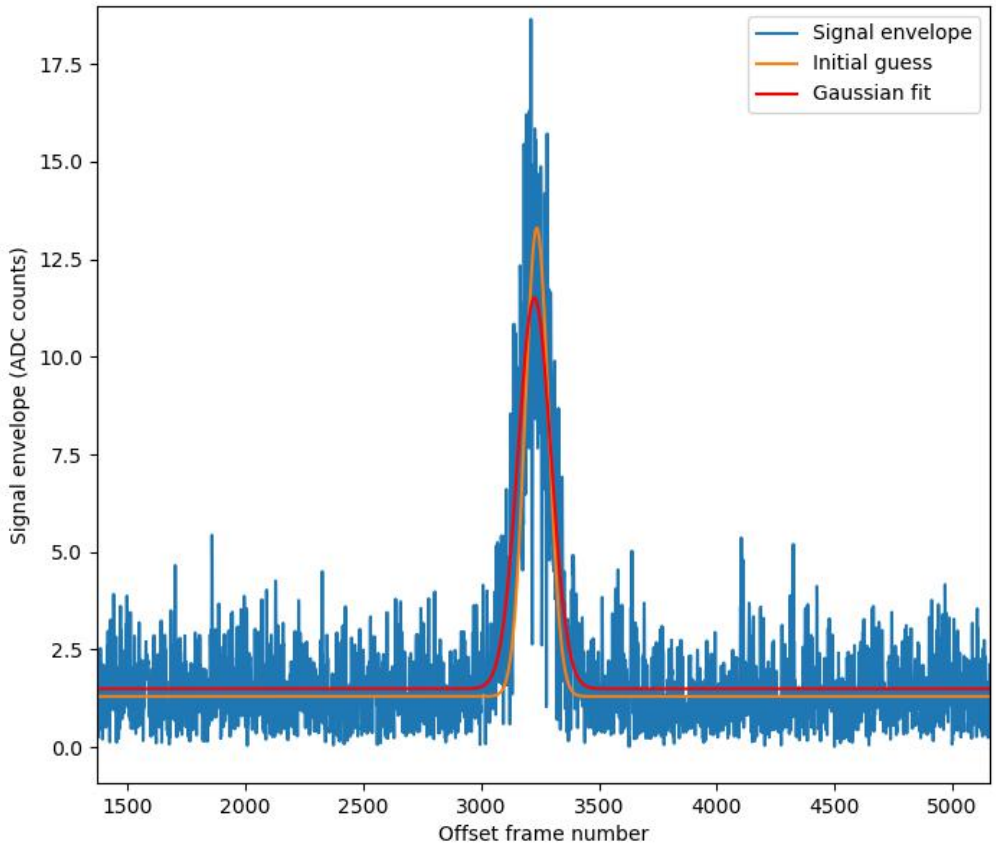

Figure 6-5: Plot for coherence length calculation.

The coherence length of a Gaussian envelope may be defined in different ways depending on how the width of the coherence envelope is specified. Two common definitions are the full width at half maximum (FWHM), which gives the width at 50% of the peak value, and the full width at the $1/e$ level. For a Gaussian with standard deviation σ, these are given by

$$\text{FWHM} = 2\sqrt{2\ln(2)}\,\sigma \tag{6.1}$$

$$\text{Full Width}_{1/e} = 2\sqrt{2}\,\sigma \tag{6.2}$$

The corresponding one-sided $1/e$ width from the center is

$$w_{1/e} = \sqrt{2}\,\sigma \tag{6.3}$$

In the present case, these widths were first determined in units of frames and then converted to axial distance using the scan speed and acquisition rate:

$$1 \text{ frame} = \frac{3.25\ \mu\text{m/s}}{40.00273 \text{ frames/s}} = 0.08124\ \mu\text{m} \tag{6.4}$$

Using this conversion, the coherence length values are

$$\text{FWHM} = 117.74 \text{ frames} \times \frac{3.25\ \mu\text{m/s}}{40.00273 \text{ frames/s}} = 9.57\ \mu\text{m} \tag{6.5}$$

$$\text{Full Width}_{1/e} = 141.42 \text{ frames} \times \frac{3.25\ \mu\text{m/s}}{40.00273 \text{ frames/s}} = 11.49\ \mu\text{m} \tag{6.6}$$

and the corresponding one-sided $1/e$ width is

$$w_{1/e} = 70.71 \text{ frames} \times \frac{3.25\ \mu\text{m/s}}{40.00273 \text{ frames/s}} = 5.74\ \mu\text{m} \tag{6.7}$$

From this, the kernel length was determined so that the sigma for the Hanning window matched that of the Gaussian fit. This number needed to make the Hanning window the correct length so that the Gaussian inside the Hanning window had the right sigma (width) value turns out to be 236. The code requires an odd number so a kernel of length 235 was used to to create a matched filter.

6.1.3 Potential Application

The ability to perform this mirror scan is important because it lays the groundwork for future measurements of mirror surface quality, including quantitative assessments of flatness such as $\lambda/10$. In precision interferometric systems, mirror surface errors can degrade wavefront quality, introduce optical misalignment, and increase measurement uncertainty. This is particularly relevant in high-accuracy metrology platforms such as the NIST-4 Kibble balance, where optical interferometry is used in experiments that realize the kilogram under the modern SI definition based on the fixed numerical value of the Planck constant. Accurate characterization of mirror flatness is therefore important for supporting the low-uncertainty optical measurements required in high-precision metrology.

6.2 Step Height Validation Sample

I additionally machined a step height validation sample I modeled with a stepdown of 20 um per step. Each cylinder had a diameter 1 mm larger than the previous one. I laser cut an aluminum sheet to size using the xTool MetalFab Laser Welder and then CNC milled the part on the Hurco VMX42SRTi 5 Axis Machining Center with help from Dan and Colin.

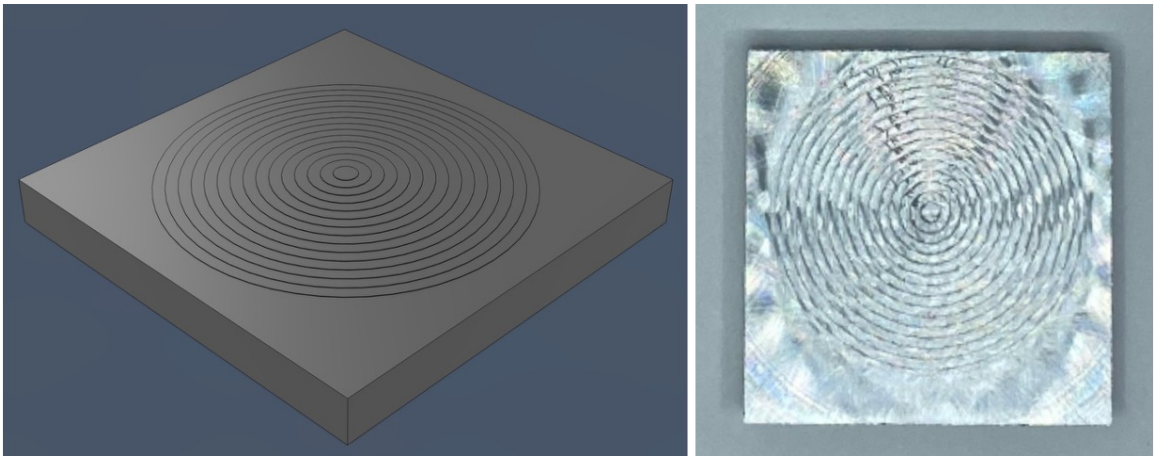

Figure 6-6: Step height validation sample with CAD file (left) and photo (right).

I scanned the sample using the optical profilometer, which yielded the following slightly

tilted height map.

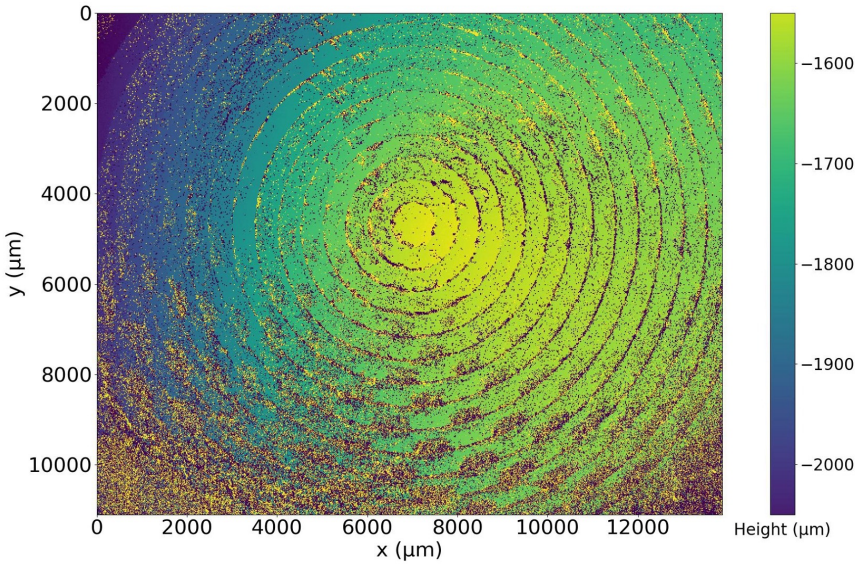

Figure 6-7: Step height validation sample height map.

Taking a row and column of pixels that pass through the center of the sample yields the following result.

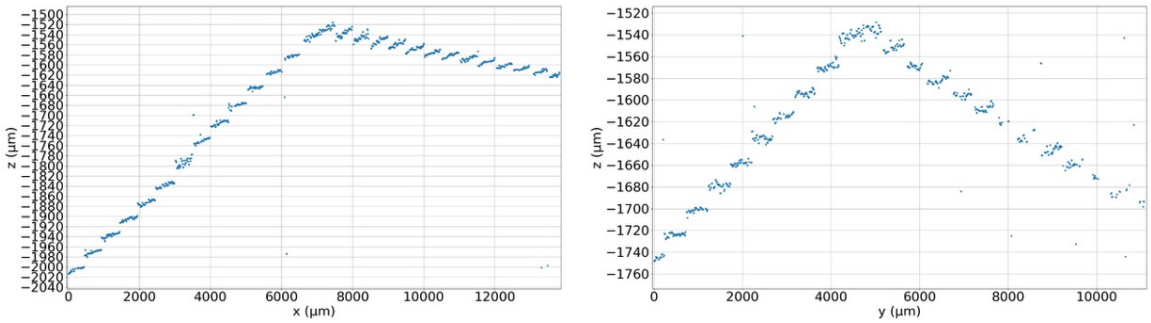

Figure 6-8: Step height validation sample plots (raw data).

To remove the tilt, I measured the slope between the outermost matching steps and applied the correction to the x and y coordinates for the two respective plots. From the geometry of the plots, the tilt angle along the x axis is approximately 1.6° and the tilt angle along the y axis is approximately 0.3°, which are sufficiently small for the small angle approximation to be valid here.

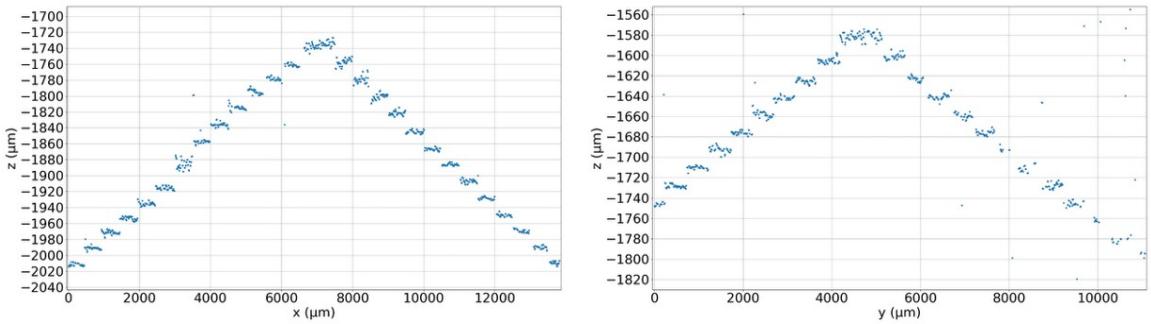

Figure 6-9: Step height validation sample plots (tilt-corrected).

As is shown in Figure 6-9, the optical profilometer measured the steps to be approximately 19 um, just shy of the modeled 20 um. I suspect this is due to the quantization of the z-axis encoder in the Hurco VMX42SRTi 5 Axis Machining Center used to fabricate the sample. While the exact quantization does not appear to be disclosed in datasheets, the quoted positioning accuracy of the milling machine is 10 um with a repeatability of 5 um, which is consistent with this result.

6.3 Dime

This next sample is a dime. As shown in the figure below, it recovers the overall geometry rather well. The scale bar is the same for both height maps. The image on the left shows the height map with all of the noise kept in, and the image in the center has been thresholded such that the pixels darker than the darkest real surface and brighter than the brightest real surface are set to the minimum value. Comparing these two images shows that the noise in the raw height map data can be attributed to a combination of low reflectivity in some regions and the so-called "batwing effect" which occurs when light reflected from the surface is scattered at too large of an angle to enter the optical system, making it appear dark. This highlights the importance of tailoring image processing methods to the specific targets being imaged in order to achieve better results.

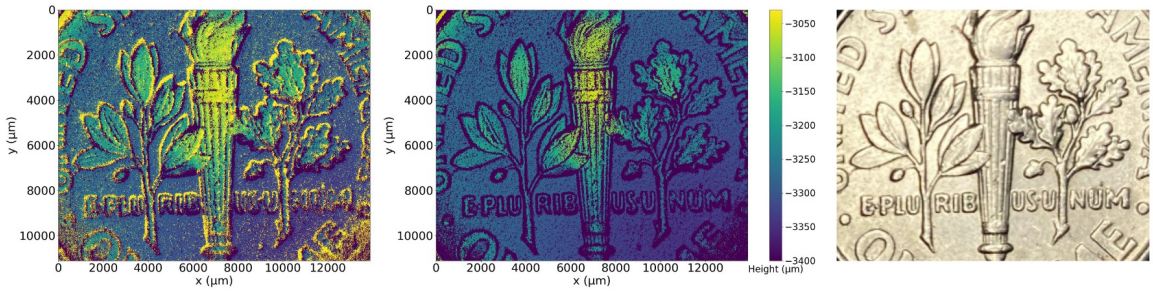

Figure 6-10: Dime scan results. Raw height map (left), height map after flying pixel removal (center), and photograph of dime back (right).

Raised surfaces are depicted with increasingly lighter colors, whereby the the torch's flame and the rim of the dime in the top left appear yellow in the height map. Edge regions, such as those surrounding letters and forms, suffer from a batwing effect, meaning that they reflect light at an angle that is too high to be captured by the lens used here. Likewise, the dime surface has surface defects such as small pockets which reflect light at extreme angles that miss the objective's acceptance cone, leading to the smattering of dark pixels in the image. In future iterations, a higher NA lens can be used to capture information from more of these surfaces and improve the signal-to-noise ratio. As mentioned in a previous section, there is also substantial compression noise due to the video acquisition. Additional processing can be performed to reduce the effects of these, such as by creating a mask that allows outlier pixels to be flagged, followed by replacing them using a nearest-neighbor-informed smoothing algorithm. More remains to be done here.

6.4 Vickers Hardness

I additionally scanned some Vickers hardness samples. Vickers hardness is determined based on the mean diagonal length of the indentation. A sample made of 1/8"-thick polished 6061 T6 aluminum[30] was prepared in The Laboratory for Physical Metallurgy (MetLab) with guidance from Shaymus Hudson using the Struers/Emco-Test DuraScan 70 Vickers Hardness Tester with a 20X objective, 0.45 NA lens, 5 mm indentation spacing, and dwell time of 15 seconds in accordance with ASTM E92-17[31]. 16 indentations were performed

with different force parameters.

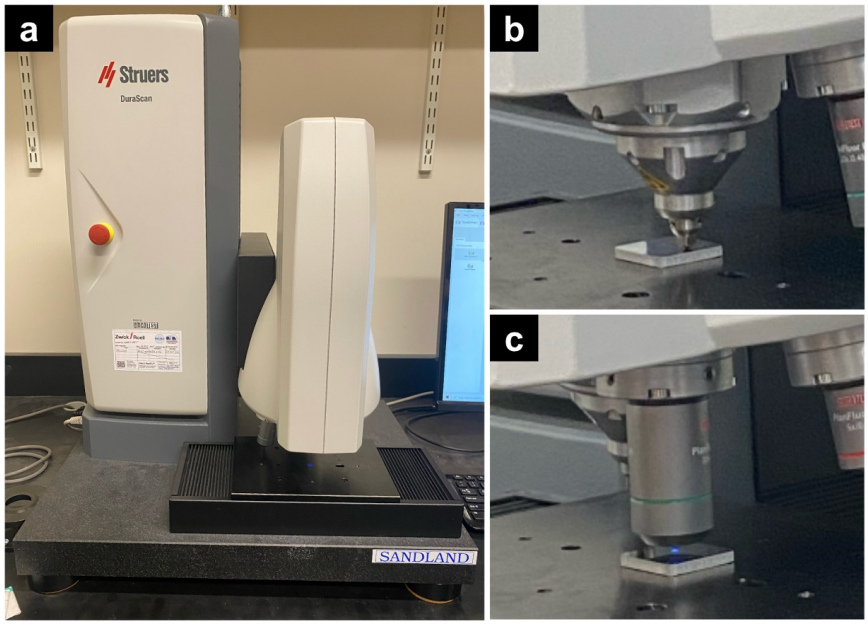

Figure 6-11: Vickers hardness test setup. (a) Struers/Emco-Test DuraScan 70 Vickers Hardness Tester with (b) a zoomed-in view of the indentation and (c) microscopy measurement steps.

The sample's Vickers hardness was calculated from automated measurement of the two diagonals and plugging into the Vickers hardness formula (Equation (6.8)). Wherever the automated edge detection struggled, the edge positions were manually selected for measurement. This yielded an average HV of 110.688 kg-f with a standard deviation of 4.078. I have included a few representative indentations here.

$$HV = 1.8544 \frac{F}{\left(\frac{d_1+d_2}{2}\right)^2} \tag{6.8}$$

Using this standard method on six of the indentations made with different applied forces, HV was calculated to be 108 with a standard deviation of 2.3, which is consistent with listed material specifications. Using my optical profilometer, the diagonals were measured and a similar calculation was performed. The dark pixels did not form a clear diamond shape characteristic of Vickers hardness indents, so I measured the diagonals from edge to edge

at the center of the vertical and horizonal directions, respectively, favoring connected dark pixels over floating ones. This is definitely a high source of error in these measurements which can be improved with higher SNR in future iterations.

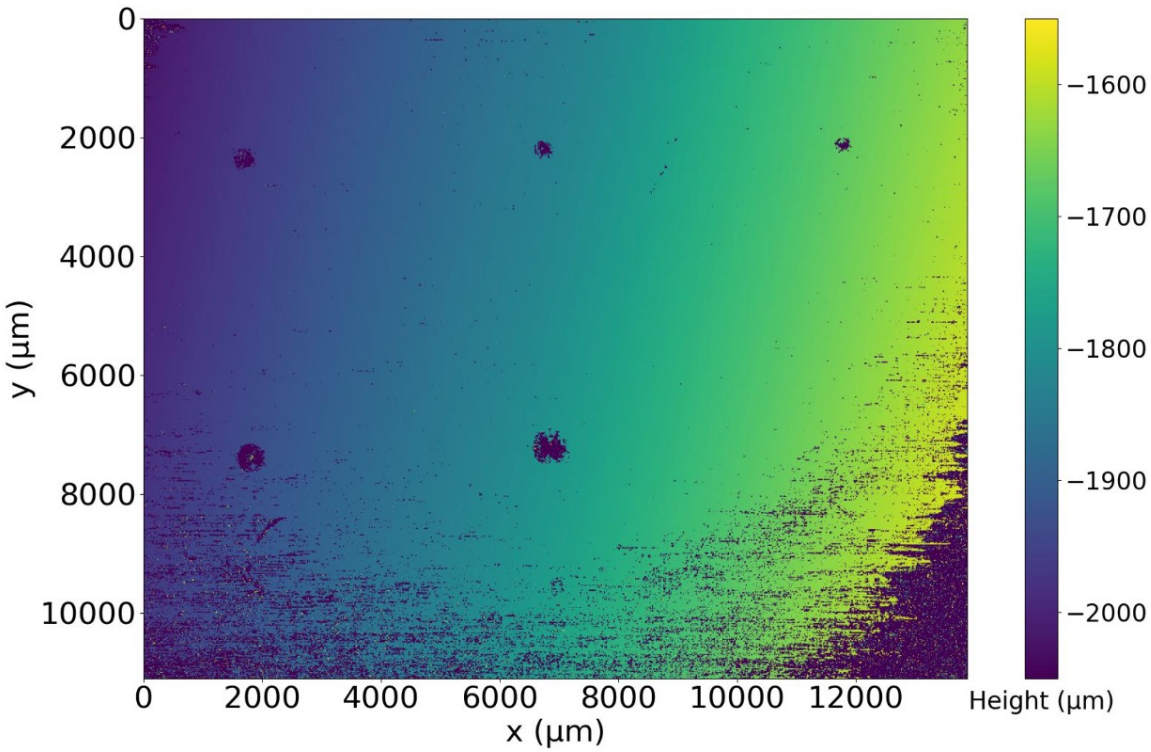

Figure 6-12: Height map of Vickers hardness polished aluminum samples after flying pixel removal.

Figure 6-12 shows six indentations. From left to right, the top row's indentations used 3, 2.5, and 2 kgf, respectively, and the bottom row's indentations used 5, 10, and 0.05 kgf, respectively, with the smallest conventionally-measured diagonal at around 28 um in the bottom-right. Because the indented portion of the material reflects light at a high angle, it misses the aperture and is recorded as a dark pixel. However, since the edges of the indentation also deflect light at a large angle, the effective dark region is larger than the outline of the indentation itself. This leads to an overestimated hole size, which resulted in HV to be calculated as 62 with a standard deviation of 15.7, representing a 42% hardness underestimation error.

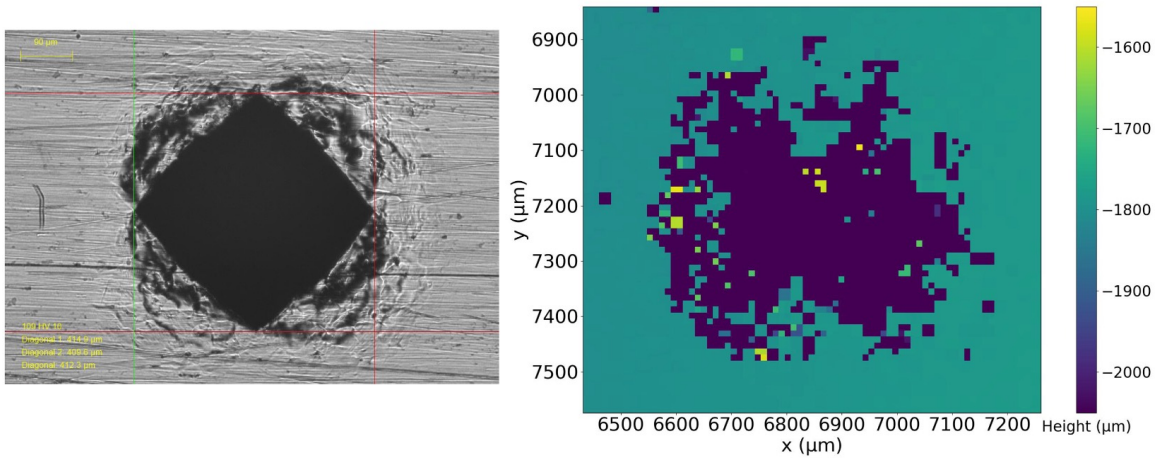

Figure 6-13: Comparison between Vickers hardness test result and optical profilometer image of HV10 sample.

Figure 6-13 shows the plastic deformation around the indentation on the aluminum's surface which is largely responsible for the low reflectivity in the regions surrounding the indent itself. I attempted a similar measurement using our lab's Rigaku CT Lab HX130 which has a voxel size of 2.1 um and spatial resolution of 5 um in its highest-resolution geometry, but the Vickers indentations were not clearly discernible in the aluminum sample. This is likely due to the shallow depth of the indents relative to the achievable voxel size and the limited x-ray attenuation contrast of aluminum. Although my optical profilometer has potential for use in characterizing hardness test samples and similar small-scale 3D structures, this experiment underscores the need for a higher power density light source and the use of a higher NA lens for larger-angle light collection to make these measurements comparable to the state-of-the-art.

Based on these results, the system performance could be improved by using a higher NA lens which could capture light at higher scattering angles, thus reducing the "batwing effect," along with introducing a higher power density light source to both increase FPS and SNR in dark regions. Additionally, the mirror test results show that there is still a micron-scale wobble, which should be addressed either by improved mechanical design or by actively measuring the true displacement of the system in real time such as with a laser interferometer, to be subtracted out during processing.

Chapter 7

Conclusions

In response to the need for affordable 3D surface profilometry with nanometer-scale axial resolution, this thesis set out to develop a high-performance white-light-interferometry-based optical profilometer at substantially lower costs than existing systems. The results demonstrate that this objective is feasible in practice, with a functioning WLI-based optical profilometer successfully designed, built, and demonstrated over the course of this work.

System	Axial Res. (μm)	Lateral Res. (μm)	FOV (mm^2)	Axial Travel (mm)	Scan Speed (μm/s)	Price ($)
THIS WORK	**0.27**	**10.8**[a]	**14 × 11**	**20**	**3.25 – 6.5**[b]	**2.5k**

[a] the image sensor sets the resolution limit here; the physics limit is a spot size of $d_{\text{spot}} = 4.2$ μm

[b] half-Nyquist to Nyquist

Table 7.1: Performance and cost metrics of the optical profilometer in this work.

The primary goal of the thesis was to establish a working system, and that goal was achieved, yielding performance metrics shown in Table 7.1 at a substantially lower cost of $2.5k as compared with the least expensive commercial option priced at $40k shown in Table 1.1.

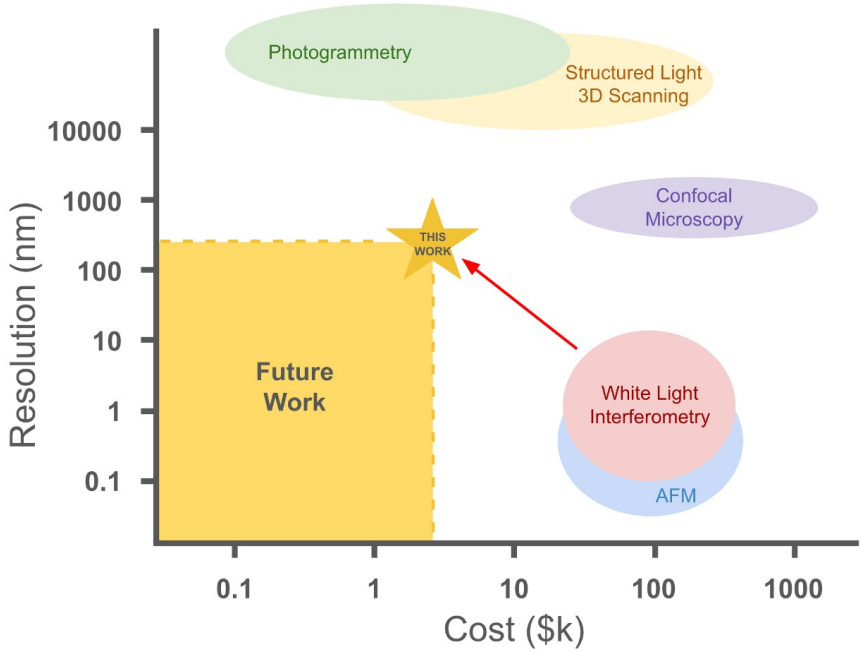

Figure 7-1: Positioning this work.

In this way, the present work begins to address the previously overlooked region of high-resolution, low-cost optical profilometry identified in Figure 7-1 and establishes a clear path toward further advances in accessible, high-performance metrology.

7.1 Next Steps

With the foundation of a low-cost white-light interferometry system now in place, future work can focus on further reducing cost and improving resolution through continued refinement of both the instrument design and the post-processing pipeline.

First, increasing the total number of photons that reach the camera would allow less reflective samples to be measured at higher frame rates by improving the signal-to-noise ratio. To accomplish this, a higher power-density light source can be used to increase the total photon budget of the system. Some preliminary work has been done in this area, but much remains to be explored, particularly in identifying a source that provides sufficient brightness from a small enough emission region while maintaining the low temporal coherence

required for white-light interferometry. Likewise, photon efficiency can be improved by replacing the current non-polarizing epi-illumination beamsplitter and achromatic doublet with one high-NA lens per arm following the polarizing beamsplitter cube. Here, the polarizing beamsplitter cube would be used for epi-illumination. In addition, adding a linear polarizer between the pinhole and the polarizing beamsplitter cube would allow the fringe contrast to be maximized at the camera without excessively blocking light further along the beam path, as is done currently.

Beyond the optical path, a more suitable monochrome camera should be selected to better match the requirements of white-light interferometry. Important camera specifications include high sensor resolution, high frame rate, and high dynamic range. To accompany this hardware change, custom camera capture code can be developed to enable lossless image acquisition and storage, as well as synchronized stage motion and frame capture. This would eliminate noise introduced by video compression and make processing substantially faster.

The signal processing code can also be improved to make the height recovery pipeline more reliable across different sample types and signal-to-noise ratios. Future work should focus on cleaning the raw measurement data and improving how the surfaces are reconstructed and visualized. Improvements could include confidence maps for identifying low-quality pixels, sub-frame interpolation of the coherence peak, better methods for identifying and repairing missing and low-SNR regions, and more sparsity-tolerant rendering techniques such as point clouds.

In parallel, the mechanical design and packaging of the system should be improved so that the instrument is easier to align, operate, and reproduce. The current prototype demonstrates the core measurement principle, but deployment would require a more enclosed and stable instrument. Future versions could include a rigid optical enclosure, a method for repeatable component alignment, and an x-rotation-constrained linear motion stage. Beyond this, using a point interferometer to measure the sample position directly would close the motion system loop and allow any remaining system wobble to be accounted for in a post-processing step.

Near-term applications for this work include Vicker's hardness indentation samples using higher-NA lenses suitable for the indentation angle, assessing machining surface quality, and imaging tiny 3D structures such as MEMS and microfluidic devices. Ultimately, this work lays the foundation for a practical, low-cost metrology tool that brings high-resolution surface measurement within reach, advancing the broader goal of expanding access to precision metrology.

References

[1] Zhenzhou Wang. "Review of real-time three-dimensional shape measurement techniques". In: *Measurement* 156 (May 2020), p. 107624. ISSN: 0263-2241. DOI: 10.1016/j.measurement.2020.107624. URL: https://www.sciencedirect.com/science/article/pii/S0263224120301615 (visited on 04/10/2026).

[2] Young-Sik Ghim and Angela Davies. "Complete fringe order determination in scanning white-light interferometry using a Fourier-based technique". EN. In: *Applied Optics* 51.12 (Apr. 2012). Publisher: Optica Publishing Group, pp. 1922–1928. ISSN: 2155-3165. DOI: 10.1364/AO.51.001922. URL: https://opg.optica.org/ao/abstract.cfm?uri=ao-51-12-1922 (visited on 04/10/2026).

[3] Peter de Groot. "Principles of interference microscopy for the measurement of surface topography". EN. In: *Advances in Optics and Photonics* 7.1 (Mar. 2015). Publisher: Optica Publishing Group, pp. 1–65. ISSN: 1943-8206. DOI: 10.1364/AOP.7.000001. URL: https://opg.optica.org/aop/abstract.cfm?uri=aop-7-1-1 (visited on 04/10/2026).

[4] *Pro.Surf: Large area optical profiler for quality control*. en. URL: https://www.polytec.com/en/surface-metrology/optical-profilometers/large-area-optical-profiler/pro-surf (visited on 04/05/2026).

[5] *Zeta-20 Optical Profilometer — 3D Optical Microscope — KLA Instruments*. en. URL: https://www.kla.com/products/instruments/optical-profilers/zeta-20 (visited on 04/05/2026).

[6] *ContourX-100*. en. URL: https://www.bruker.com/en/products-and-solutions/test-and-measurement/3d-optical-profilers/contourx-100.html (visited on 04/05/2026).

[7] *Compact white-light interferometer*. en. URL: https://www.polytec.com/en/surface-metrology/optical-profilometers/large-area-optical-profiler/metro-lab (visited on 04/06/2026).

[8] *MSE PRO 3D Optical Surface Profilometer with 220x220mm Table Size*. en. URL: https://www.msesupplies.com/products/mse-pro-3d-optical-surface-profilometer-with-220x220mm-table-size-1-85-m-s-scanning-speed (visited on 04/05/2026).

[9] *Micro.View – compact 3D surface roughness profiler — Polytec*. en. URL: https://www.polytec.com/en/surface-metrology/optical-profilometers/microscope-based-surface-profiler/micro-view (visited on 04/05/2026).

[10] *Filmetrics Profilm3D and Profilm3D-200 Optical Profilometers — White Light Interferometry (WLI) — KLA Instruments*. en. URL: https://www.kla.com/products/instruments/optical-profilers/profilm3d (visited on 04/05/2026).

[11] Sanghoon Kim et al. "Design and implementation of a low-cost, portable OCT system". EN. In: *Biomedical Optics Express* 9.3 (Mar. 2018). Publisher: Optica Publishing Group, pp. 1232–1243. ISSN: 2156-7085. DOI: 10.1364/BOE.9.001232. URL: https://opg.optica.org/boe/abstract.cfm?uri=boe-9-3-1232 (visited on 04/06/2026).

[12] *OQ LabScope*. en-US. URL: https://www.lumedica.com/oq-labscope (visited on 04/06/2026).

[13] Wan Wang et al. "High-Performance, Low-Cost Optical Coherence Tomography System Using a Jetson Orin Nano for Real-Time Control and Image Processing". In: *Translational Vision Science & Technology* 14.3 (Mar. 2025), p. 24. ISSN: 2164-2591. DOI: 10.1167/tvst.14.3.24. URL: https://pmc.ncbi.nlm.nih.gov/articles/PMC11951056/ (visited on 04/06/2026).

[14] *5.4: Coherence*. en. Jan. 2022. URL: https://phys.libretexts.org/Bookshelves/Optics/BSc_Optics_(Konijnenberg_Adam_and_Urbach)/05%3A_Interference_and_coherence/5.04%3A_Coherence (visited on 04/08/2026).

[15] Risto Montonen et al. "System spectrum conversion from white light interferogram". EN. In: *Optics Express* 25.11 (May 2017). Publisher: Optica Publishing Group, pp. 12090–12099. ISSN: 1094-4087. DOI: 10.1364/OE.25.012090. URL: https://opg.optica.org/oe/abstract.cfm?uri=oe-25-11-12090 (visited on 04/06/2026).

[16] *Superluminescent diodes — SLD — MEETOPTICS*. URL: https://www.meetoptics.com/light-sources/incoherent-sources-and-single-emitters/super-luminescent-diodes?sort_a=Price__u_USD__t_r&categories__t_s=Lasers%20%26%20Light%20Sources%3E%3E%3EIncoherent%20Sources%20%26%20Single%20Emitters%3E%3E%3ESuper-Luminescent%20Diodes%20%28SLDs%29%3E%3E%3EVisible%20SLD (visited on 04/18/2026).

[17] *Thorlabs · PF10-03-P01 Ø1" Protected Silver Mirror*. URL: https://www.thorlabs.com/item/PF10-03-P01 (visited on 04/20/2026).

[18] *Thorlabs · SLD650T 650 nm, 10 mW, TO-56, H Pin Code, Superluminescent Diode*. URL: https://www.thorlabs.com/item/SLD650T (visited on 04/18/2026).

[19] *LZ1-00R102-0000*. en-us. URL: https://www.digikey.com/en/products/detail/ams-osram-usa-inc/LZ1-00R102-0000/5032283 (visited on 04/06/2026).

[20] *LZ1-00B202-0000*. en-us. URL: https://www.digikey.com/en/products/detail/ams-osram-usa-inc/LZ1-00B202-0000/5032278 (visited on 04/06/2026).

[21] *GW CSSRM3.PM-N7P1-A434-1-700-R33*. en-us. URL: https://www.digikey.com/en/products/detail/ams-osram-usa-inc/GW-CSSRM3-PM-N7P1-A434-1-700-R33/13625152 (visited on 04/06/2026).

[22] *Fundamentals of Lasers*. en. URL: https://www.edmundoptics.com/knowledge-center/application-notes/lasers/fundamentals-of-lasers/ (visited on 04/06/2026).

[23] *LT3080 Low Dropout Regulator*. en-us. URL: https://www.digikey.com/en/product-highlight/l/linear-tech/lt3080 (visited on 04/06/2026).

[24] *Final Project*. URL: https://fab.cba.mit.edu/classes/863.25/people/SaraFernandez/final/index.html (visited on 04/22/2026).

[25] *Properties of Sapphire - Meller Optics - Over 100 Years of Excellence*. en-US. Oct. 2021. URL: https://melleroptics.com/properties-of-sapphire/ (visited on 04/08/2026).

[26] *modular-things.com/things/stepper-hbridge-xiao/*. URL: https://modular-things.com/things/stepper-hbridge-xiao/ (visited on 04/20/2026).

[27] Jake Robert Read et al. "Modular-Things: Plug-and-Play with Virtualized Hardware". en. In: *Extended Abstracts of the 2023 CHI Conference on Human Factors in Computing Systems*. Hamburg Germany: ACM, Apr. 2023, pp. 1–6. ISBN: 978-1-4503-9422-2. DOI: 10.1145/3544549.3585642. URL: https://dl.acm.org/doi/10.1145/3544549.3585642 (visited on 04/20/2026).

[28] Neil A. Gershenfeld. *The physics of information technology*. eng. 1. paperback ed. Cambridge series on information and the natural sciences. Cambridge: Cambridge Univ. Press, 2011. ISBN: 978-0-521-21022-5.

[29] *PYTHON1300*. en. URL: https://www.onsemi.com/products/sensors/image-sensors/python1300 (visited on 04/19/2026).

[30] *McMaster-Carr*. en. URL: https://www.mcmaster.com/ (visited on 04/15/2026).

[31] *compass*. URL: https://compass.astm.org/content-access?contentCode=ASTM%7CE0092-17%7Cen-US (visited on 04/15/2026).